UNIVERSITY OF CALIFORNIA,

IRVINE

Superlattice Fabrication for Designer Mesoscale Quantum Dot Solids

DISSERTATION

submitted in partial satisfaction of the requirements

for the degree of

DOCTOR OF PHILOSOPHY

in Chemical and Biochemical Engineering

by

Caroline Yu Qian

Dissertation Committee:
Professor Matt Law, Chair
Assistant Professor Stacy Copp
Assistant Professor Erdem Sasmaz

2022

DEDICATION

To

My parents, who are always enthusiastic in their encouragement of whatever I set my mind to,

And my sister, who is always the voice of intelligence and reason regardless of her age:

I love you all very much.

CONTENTS

LIST OF FIGURES

LIST OF TABLES

ACKNOWLEDGEMENTS

I would first like to thank Prof. Matt Law for advising my research these past six years. I appreciate the effort you put into teaching me to be a thorough researcher and independent problem solver; regardless of what lies ahead in the decades to come, I am confident in my abilities to face it all. Thank you also to my advancement and dissertation committee members for your time and interest in my research.

Thank you to all of the Law Lab members, past and present. A special thanks to Alex Abelson and your years spent patiently guiding and tirelessly working with me on the quantum dot superlattice project; to Yash Gargasya and Andy Yang for the hours of conversation, scientific or otherwise – lab life mid-pandemic wouldn't have been nearly as bearable without you; and to Geemin Kim, who will carry on the quantum dot legacy!

Thank you to my family for all of their love, even from thousands of miles away, and to each of my friends – whether we met as kindergarteners or not until after I had fled the Midwest, I could not have completed this degree without your wholehearted support (and sometimes, necessary distraction).

VITA

CAROLINE YU QIAN

2016	B.E. in Chemical Engineering, University of Minnesota - Twin Cities
	B.Sc. in Chemistry, University of Minnesota - Twin Cities
2017	Master's in Chemical and Biochemical Engineering, University of California, Irvine
2022	Ph.D. in Chemical and Biochemical Engineering, University of California, Irvine

FIELD OF STUDY

Fabrication and characterization of PbSe quantum dot superlattices

PUBLICATIONS

1. Qian, C., Abelson, A., Miller-Casas, A., et al. Photobase-triggered formation of 3D epitaxially-fused quantum dot superlattices with high uniformity and low bulk defect densities. *ACS Nano*, 16, 3239-3250 (2022).
2. Kavrik, M. S., Hachtel, J., Ko, W., Qian, C., et. al. Emergence of distinct electronic states in epitaxially-fused PbSe quantum dot superlattices. Preprint (2021).
3. Hansen, C., Unruh, Dl, Alba, M., Qian, C., et al. Hierarchical carrier transport simulator for defected nanoparticle solids. *Scientific Reports*, 11, 7458 (2021).
4. Chu, X., Heidari, H., Abelson A., Unruh, D., Hansen, C., Qian, C., et al. Structural characterization of a polycrystalline epitaxially-fused colloidal quantum dot superlattice by electron tomography. *Journal of Materials Chemistry A*, 8, 18254-18265 (2020).

5. Ueda, S. T., Kwak, I., Abelson, A., Wolf, S., Qian, C., et. al. Electronic passivation of PbSe quantum dot solids by trimethylaluminum vapor dosing. *Applied Surface Science*, 513, 148512 (2020).
6. Abelson, A.*, Qian, C.*, et al. Collective topo-epitaxy in the self-assembly of a 3D quantum dot superlattice. *Nature Materials*, 19, 49-55 (2020).
7. Geremew, A., Qian, C., et. al. Low-frequency electronic noise in superlattice and random-packed thin films of colloidal quantum dots. *Nanoscale*, 11, 20171-20178 (2019).
8. Wang, Y., Peng, X., Abelson, A., Xiao, P., Qian, C., et. al. Dynamic deformability of individual PbSe nanocrystals during superlattice phase transitions. *Science Advances*, 5 (2019).
9. Wang, Y., Peng, X., Abelson, A., Zhang, B.-K., Qian, C., et. al. In situ TEM observation of neck formation during oriented attachment of PbSe nanocrystals. *Nano Research*, 1-5 (2019).
10. Peng, X., Abelson, A., Wang, Y., Qian, C., et. al. In situ TEM study of the degradation of PbSe nanocrystals in air. *Chemistry of Materials*, 31, 190-199 (2018).

*co-first author

ABSTRACT OF THE DISSERTATION

Superlattice Fabrication for Designer Mesoscale Quantum Dot Solids

by

Caroline Yu Qian

Doctor of Philosophy in Chemical and Biochemical Engineering

University of California, Irvine, 2022

Professor Matt Law, Chair

Colloidal quantum dot (QD) solids have long been considered a promising nanomaterial, combining the wide range of material property-tuning capabilities associated with the nanoscale and the potential for comparable performance in optoelectronic and photovoltaic applications to those of a conventional bulk material. However, most research in this field focuses on amorphous QD solids, the extremely short-range order of which greatly hinders charge transport within the film. To counter this, we have developed a fabrication method for three-dimensional PbSe QD superlattices that utilizes self-assembly on a liquid subphase, as well as photo-triggered formation of the desired epitaxially-fused superlattice (epi-SL). These epi-SLs possess high spatial order, with crystalline grains on the micron length scale, and carrier mobilities several orders of magnitude higher than that of an amorphous QD film. Combining this with atomic layer deposition infilling will passivate any remaining defect states within the epi-SL, eventually triggering mini-band formation and achieving delocalized charge transport similar to that observed in bulk semiconductors.

INTRODUCTION

Quantum dots (QDs) have held research interest for decades because of their unique photophysical properties. QDs are nanoparticles that are smaller than twice the Bohr radius of the excitons in the bulk material; due to their small size (2-20 nm), they experience quantum confinement in three dimensions.[1,2] As a result, QDs possess discrete electronic states, earning them the nickname of "artificial atoms". Through control of their size and surface chemistries, QDs can be finely tuned to display various optical, chemical, and electronic properties, making their three-dimensional assemblies a solution-processable and cost-effective alternative to bulk semiconductors.

However, there remain serious barriers to the QD's potential as a nanoscale building block for a semiconductor material. Most QD films that are more than one monolayer of particles thick have been fabricated using methods that produce solids with zero (i.e., amorphous) or only short-range spatial order, i.e., polycrystalline films with grain sizes <250 nm. These grain sizes are further reduced during the ligand exchange process, during which the insulating surface ligands the QDs are synthesized with are removed and/or replaced with shorter, sometimes more conductive ligands in order to bring neighboring QDs close enough to electronically couple and facilitate charge transport. The physical result of this coupling is decreased distance between the QDs and necking, i.e. fusion, of the nanoparticles to each other, further reducing the original volume of the QD film. Thus, the contraction that results from the ligand exchange process often results in an unavoidable and abundant distribution of cracks and other mechanical defects throughout the solid.

There also exist many chemical barriers to charge transport; QD films suffer from surface defects, including dangling bonds and missing atoms, as well, which cause trap states that lower charge mobility and prevent band transport. QDs are also air-sensitive, although stability can be achieved in a variety of ways, including by atomic layer deposition, polymer encapsulation, and certain ligand treatments. These methods not only serve to protect the device from oxygen exposure, but can also affect and even improve the resulting electronic properties.

The following dissertation will focus on research surrounding the issues of both low spatial order from small grain sizes, as well as high energy disorder from surface defects, in order to produce a three-dimensional QD solid with potential for practical semiconductor applications. By combining high spatial order of a three-dimensional QD superlattice with low energy disorder from surface passivation, we can produce a QD solid that exhibits the band transport characteristic of bulk semiconductor materials. Specifically, this can be achieved by utilizing a self-assembly method for fabricating QD films, combined with atomic layer deposition as a passivation technique. Routine characterization mainly involves Fourier-transform infrared spectroscopy (FTIR) and scanning electron microscopy (SEM) for evaluation of ligand exchange and morphology, respectively, and field-effect transistor (FET) measurements to extract carrier mobilities.

Lead chalcogenide QDs are of particular interest as semiconductor nanoparticles due to their large Bohr radius, high charge mobility, and capacity for multiple exciton generation.[2] This research will focus on PbSe QDs in particular, as they have stronger electronic coupling capabilities than PbS due to their larger size, and thus larger Bohr radius, and can maintain relative stability, unlike PbTe.[3]

The following chapters will discuss:

1. Introductory concepts to QDs and their intricate chemistries,
2. Optimization of PbSe QD superlattice (SL) fabrication through utilization of self-assembly of the QD film on a liquid subphase – including a photo-triggered fabrication method that produces our best QD SLs to date, both in terms of chemical and structural uniformity, as well as in measured structural defect densities,
3. Tunability of various QDs self-assembly parameters, including solvent types, film thickness and grain size,
4. Development of alternative ligand exchange procedures, in-depth structural characterization of the resulting exchanged films and their grain sizes and defect distributions, and early efforts to facilitate single-grain charge transport measurements,
5. Future work to be done based on the launchpad of this body of work,
6. Important experimental methods utilized to perform the summarized research.

CHAPTER 1 : CONCEPTS IN QUANTUM DOT CHEMISTRY

1.1 QUANTUM DOT SYNTHESIS

PbSe QDs are commonly produced through colloidal synthesis by the hot-injection method, which involves the mixing of two precursors – in this case lead (II) oleate and TOP-Se (a molecular complex of trioctylphosphine and selenium) – inside a sealed, air-free vessel at elevated temperatures.[4] A full description of this procedure is described in Chapter 6.1. Briefly, the lead (II) oleate is first formed by mixing lead (II) oxide and oleic acid in octadecene (ODE). The ODE is inert and has a high boiling point, and so is safe to use as a solvent for the elevated temperatures and low pressures of the synthesis. Upon injection of the TOP-Se into the lead (II) oleate solution, the PbSe QDs will nucleate and grow until the entire reaction is quenched and cooled back down to room temperature. Depending on the reaction temperature and growth time, PbSe QDs can form a variety of sizes and shapes, with their surfaces capped by a variety of ligands besides oleate, e.g., oleylamine, depending on the precursor.[4]

While QDs are often depicted to be spherical in artistic renditions, they are faceted particles, with a distribution of {100}, {110}, and {111} facets depending on size and symmetry. Smaller PbSe QDs are truncated cuboctahedrons, and as they grow the {100} facets, i.e., faces associated with a cube, become larger until the QD becomes cuboid. For the research presented here, the PbSe QDs are grown to be 6.5 – 6.9 nm in diameter, making them truncated cuboctahedrons with a distribution of all three facet types, as seen in Figure 1.1.

The colloidal synthesis described above leaves the QDs with a surface layer of organic ligands – often long hydrocarbon chains such as deprotonated oleic acid, i.e., oleate – that ensure colloidal stability in a chosen solvent. Oleate coverage of each facet differs based on its surface energy and ratio of Pb to Se atoms exposed on that particular plane. Such ligands are often also insulating, so they must be either removed or exchanged with a shorter and/or more conductive molecule to allow electronic coupling between neighboring QDs and subsequently, charge transport through the entire QD solid. Because oleate is most likely to be removed from the {100} facets due to their low binding energy, fusion of QDs is most often observed to occur at these facets upon ligand exchange of the original surface oleate.[5] Further discussion on ligand exchange and its role in QD surface chemistry can be found in Chapter 1.3.

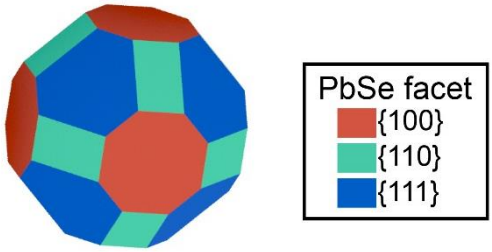

Figure 1.1: *Depiction of a typical faceted PbSe QD. As the QD size grows, the red {100} facets also enlarge, allowing the QD to approach a cuboid geometry.*

1.2 QUANTUM DOT SELF-ASSEMBLY

Most QD solids are fabricated by dip coating or spin coating methods, resulting in films that are amorphous, i.e., non-ordered, or only possess short-range order. During dip coating, the desired substrate for the film is sequentially submerged first into a solution of the QDs, followed by a solution of the desired exchange ligand, and lastly a rinse solution to cleanse the film before the entire cycle is repeated. The thickness of the film then depends on both the concentration of

the QD solution, as well as the number of dip coating cycles performed. Spin coated films, meanwhile, are often fabricated by first depositing a layer of the QD solution and static spinning, wicking away the solvent to deposit only the QDs onto the substrate, followed by a static spinning of exchange ligand solution.

Both dip and spin coating implement solid state ligand exchange, i.e., the QD solid is dry and already deposited on the desired substrate when the ligand exchange process occurs. As the original insulating ligands are removed and/or replaced during the exchange, the film contracts due to the shorter physical distance between all neighboring QDs. This sudden contraction often causes cracking and tearing in the films as the deposited QDs are forced out of their original positions, and these resultant macro-and micro-scale defects become large hindrances to any subsequent charge transport. While there are methods that have been developed to exchange the ligands on the QDs in solution, i.e., in situ, before QD deposition onto the substrate, subsequently using dip or spin coating to deposit the films still results in the same issue of low spatial order due to small grain sizes within the solid (<100 nm), even while the macroscopic cracking is largely eliminated.[4]

QD self-assembly on a liquid surface followed by Langmuir-Schaefer deposition is a third procedure that can be used to make QD solids.[6] Self-assembly of nanoparticles is a well-studied science that involves a complex interplay of physical and chemical phenomenon – including fluid dynamics, electrostatic repulsion, evaporation kinetics, and surface interactions – between nanoparticle and the surrounding solvent(s).[4,7,8] Generally, the QD solution is first deposited on a liquid subphase inside a well or dish. The QD solvent is then evaporated in a controlled manner, usually by at least partial coverage provided by the well lid, resulting in a dry QD film floating on the subphase surface. The exchange ligand, also referred to as a chemical trigger, can then be

injected into the subphase underneath the film; the injected ligand can then diffuse through the subphase and begin exchanging with the original surface ligand layer on each of the QDs within the solid, triggering oleate removal and subsequent fusion, i.e., electronic coupling, of each QD and its nearest neighbors. The resulting film is then stamp-transferred onto the desired substrate via the Langmuir-Schaefer method, after which additional treatments to remove additional oleate and passivate remaining surface defects can be performed. A detailed outline of this group's developed procedure is provided in Chapter 6.2, and Figure 1.2 depicts a schematic of the entire process as just described.

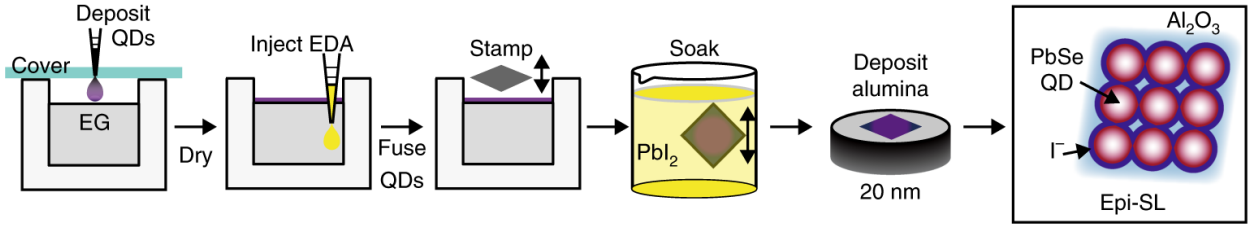

Figure 1.2*: Schematic of the epi-SL fabrication process, from self-assembly of the oleate-capped SL to the final alumina ALD coating. Material from Abelson, Qian, et. al., Collective topo-epitaxy in the self-assembly of a 3D quantum dot superlattice, Nature Materials, published 2020, Springer Nature Ltd.*

Evaluating the morphologies of QD films fabricated by any of the above methods – i.e., grain sizes, film thickness, and structural order – can be achieved through electron microscopy, particularly scanning (SEM) and transmission (TEM). Using an electron beam instead of visible light allows imaging of nanometer-sized particles, and a larger depth of field results in higher quality 3D imaging than what is achievable with an optical microscope. The resolution of an SEM image depends on a range of factors – including electron beam source, the voltage, and lens and aperture sizes. When the electron beam encounters the sample, several types of electrons can be scattered and collected at a detector to collect an image.

Secondary electrons result from inelastic scattering with electrons in the sample; upon impact by the electron beam, the sample's inner shell electrons are scattered. This then provides topographical information of the sample surface.

Backscattered electrons are from elastic scattering of the electrons by the sample nuclei; once backscattered, the electron energies can be used to show elemental differences, i.e., relative atomic masses, in the sample.

X-rays are produced after an inner shell electron in the sample is scattered to become a secondary electron. Another electron in the sample atom then fills the shell vacancy, and the energy difference is released through radiation. This results in each element having a unique X-ray fingerprint, and techniques such as energy dispersive spectroscopy (EDS) can be used to determine a sample's exact chemical composition.

In most cases, top-down (i.e., plan view) SE images gathered via SEM provide ample information about the QD film's morphology and spatial order.

TEM, meanwhile, is an even more powerful imaging technique that can achieve atomic resolution for QD samples. Because the electron beam is transmitted through the sample in this case, however, this makes TEM a less desirable method for imaging the surface morphology of a multilayer film – because there is overlap between layers of QDs, it becomes hard to distinguish individual QDs as the number of layers increases. Therefore, SEM is usually the preferred imaging method, with TEM being reserved for electron diffraction, via which diffraction patterns can reveal atomic lattice parameters,[9] and electron tomography, which rotates a disc or "needle" sample and takes images at every increment with which to reconstruct the positioning of each individual QD within that needle.[10]

After ligand exchange in a self-assembled SL, the neighboring facets of adjacent QDs fuse together. Because these facets are of the same orientation, i.e., the {100}, these exchanged films can be referred to as epitaxially-fused superlattices (epi-SLs). These films, mostly mono- or bilayers of QDs, have exhibited grain sizes on the order of 500 nm lengths after exchange.[11] Because the liquid subphase allows some flexibility during the deposition and drying of the initial oleate-caped film, as well as during the subsequent ligand exchange contraction, that solid state deposition and exchange is unable to provide, macroscopic cracking due to ligand removal/replacement is reduced and results in a significant improvement in spatial order over the films produced by the previous fabrication methods.

Much of the current published literature on self-assembled QD superlattices is research on 2D films, or monolayers. As mentioned previously, the different facets of QD nanoparticles have different surface energies due to the ratio of cations to anions on a particular facet arrangement, and thus differing amounts of oleate to be removed from the surface before fusion between neighboring QDs is possible. Because the oleate is complexed with the Pb^{2+} cation, the {100} facets have the lowest surface energy and thus are the most likely to fuse first.[12] The monolayer epi-SLs have been shown to orient in a few different ways, including a square configuration with the {100} facets facing up, i.e., parallel to the subphase surface; rows of QD chains with the {110} facets facing up; and a hexagonal structure attributed to silicene with the {111} facets facing up.[11–13] 3D films take on the same set of orientations, although with varying frequencies, and grain sizes are expected to be smaller because of the addition of a third dimension. Figure 1.3 shows examples of {100} and {110} oriented oleate-capped and PbSe QD epi-SL grains from films that are 10-11 QD layers thick (~70 nm).

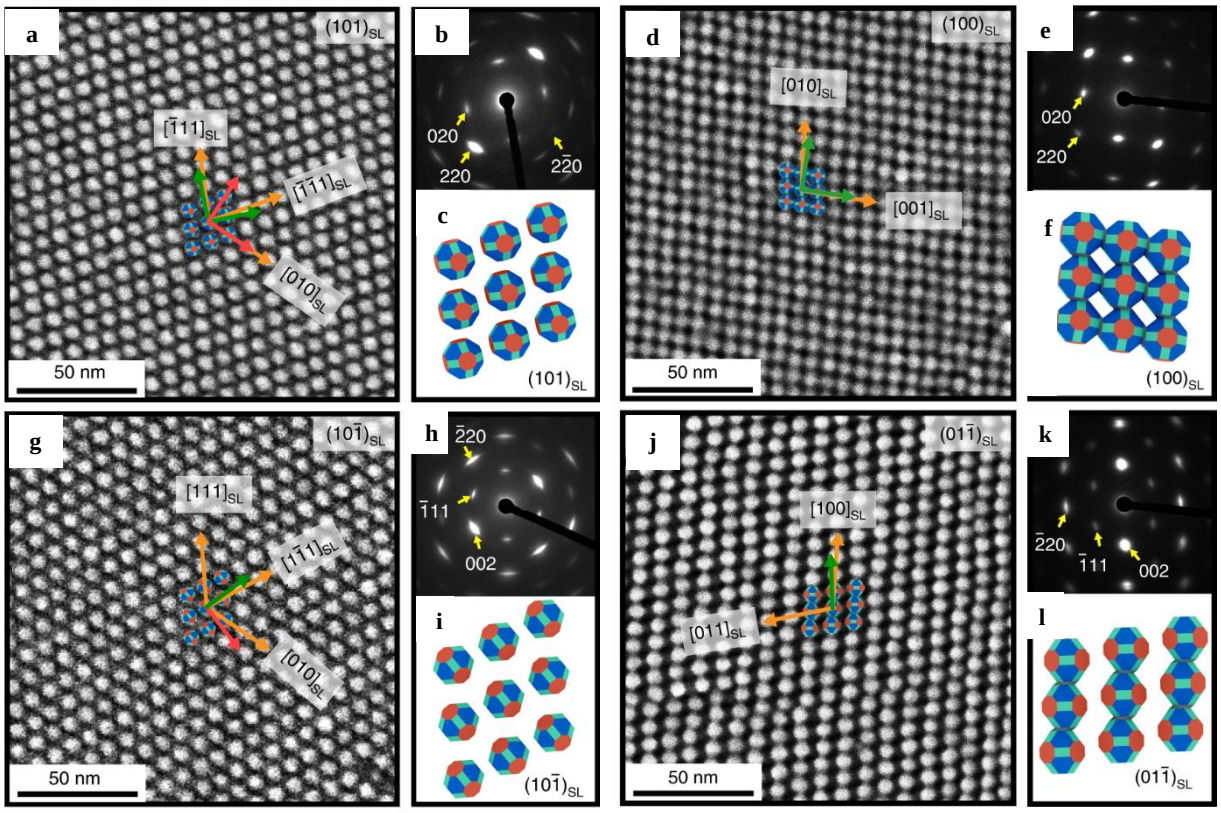

Figure 1.3: *Representative oleate-capped and epi-SL structures. a) Secondary electron image (SEI) of a (101) oriented oleate-capped SL grain. b) The corresponding selected area electron diffraction (SAED) pattern of the QD atomic lattice. c) Model of the first monolayer of QDs in this oleate-capped SL orientation. d-f) The same progression as a-c but for the (100) epi-SL orientation, which the (101) oleate-capped SL transitions into upon epi-fusion. g-i) The same progression as a-c but for the (10-1) oleate-capped SL orientation. j-i) The same progression as a-c but for the (01-1) epi-SL orientation, which the (10-1) oleate-capped SL transitions into upon epi-fusion. Material from Abelson, Qian, et. al., Collective topo-epitaxy in the self-assembly of a 3D quantum dot superlattice, Nature Materials, published 2020, Springer Nature Ltd.*

The self-assembly process is, of course, subject to a wide range of variables. First, the choice of subphase is important: it must be immiscible with and denser than the QD solvent, and nonvolatile so that it does not evaporate while the QD film is drying. Most report using ethylene or diethylene glycol towards this purpose. Second, the QD solvent evaporation rate must be

carefully controlled, as faster evaporation tends to result in uneven film thickness and morphology, as well as less spatial order; this could be because faster evaporation rates allow less time for individual QDs to find their favored spatial and energetic equilibrium on the subphase surface.[8] On the other hand, extended periods of drying, e.g. over days or weeks, can result in different superlattice orientations than those formed by shorter drying periods.[13] It should also be noted that ethylene glycol has been shown to remove oleate from the QD surface over time, although some reports claim that adding micromolar concentrations of oleic acid stabilizes the equilibrium of oleate in the subphase versus on the QD surface, and thus prevents this process.[12] Efforts to mitigate these side effects of EG as a subphase, as well as explorations into other factors of self-assembly and oleate-capped SL fabrication, are discussed in Chapters 3.1 and 3.2.

1.3 QUANTUM DOT SURFACE CHEMISTRY

The properties of a QD solid are often a function of surface chemistry. As previously described, the QDs themselves are synthesized with insulating surface oleate, which must then be exchanged or removed to physically fuse and electronically couple the QDs into a solid capable of charge transport. The QDs before exchange are also not without their surface defects, and additional ligand treatments can help passivate these trap states in the resulting films.

Ligand treatment has been shown to affect the individual QDs in terms of properties like photoluminescence, and QD films in terms of epi-SL grain orientation, morphology, and charge transport. Common ligand exchange molecules include short-chain amines (e.g., ethylenediamine), thiols (e.g., ethanedithiol), carboxylates (e.g., formate, mercaptopropanoate), and thiocyanate.[11,14,15] Successful exchange and passivation with halides (e.g., chloride, iodide) have also been reported.[16] It is also possible to combine two or more ligands in the exchange

process, either simultaneously or sequentially, in order to reap the benefits of both molecules while maintaining or improving the integrity of the resulting epi-SL.[17] QD ligand exchange occurs through one of three main pathways:

X-type: the original ligand on the QD surface, i.e., the oleate, is an anion that can be protonated. Once protonated, it can leave the surface as oleic acid, and can be replaced with the now deprotonated exchange ligand. Examples of this include iodide salts – the use of which is further discussed in Chapter 2.1 – and formic acid.[9]

L-type: the entire exchange ligand replaces the oleate by similarly chelating or complexing to the QD surface; an example of this could be a diamine, or a phosphine.

Z-type: the cation on the QD surface, i.e., the Pb^{2+}, is exchanged for another while the oleate remains nominally unexchanged.[17] Other metal cations that favor chalcogenides (i.e., Se^{2-} and others in the same group of the periodic table), such as Cd^{2+}, could be used for this.

The main ligand exchange treatment for this research focuses on ethylenediamine (EDA), although other treatments explored within the breadth of this project are reported in Chapter 4.1. The conventionally proposed mechanism for how EDA removes the oleate is described as L-promoted Z-type displacement, where the EDA acts as an L-type ligand, i.e., a neutral donor, and chelates with the Pb^{2+} on the QD surface before subsequently removing the entire Pb-oleate complex.[17]

However, an X-type ligand exchange can occur in the presence of protic solvents such as ethylene glycol (EG). The glycoxide-oleate exchange mechanism, where glycoxide is the anion analog to the EG subphase implemented in QD SL self-assembly, is also able to induce oleate removal and fusion across the crystallographically matching {100} facets, i.e., epitaxial fusion (epi-fusion).[9,18] During this process, the injected EDA acts as a Brønsted-Lowry base, i.e., a proton

acceptor, deprotonates an EG molecule in the subphase to produce glycoxide, a negatively charged ligand that can then exchange with the surface oleate to initiate epi-SL formation. This contrasts with the previously discussed L-promoted Z-type exchange, in which EDA acts as a Lewis base, i.e., an electron pair donor, to remove oleate directly. In fact, both Brønsted and Lewis mechanisms could be in effect under these conditions, although Chapter 2.2 discusses the Brønsted mechanism, i.e., the glycoxide-oleate exchange, in further depth, and explains its role as the major actor in the described protic environment. A schematic of the proposed glycoxide-oleate exchange process and subsequent epi-SL formation is shown in Figure 1.4.

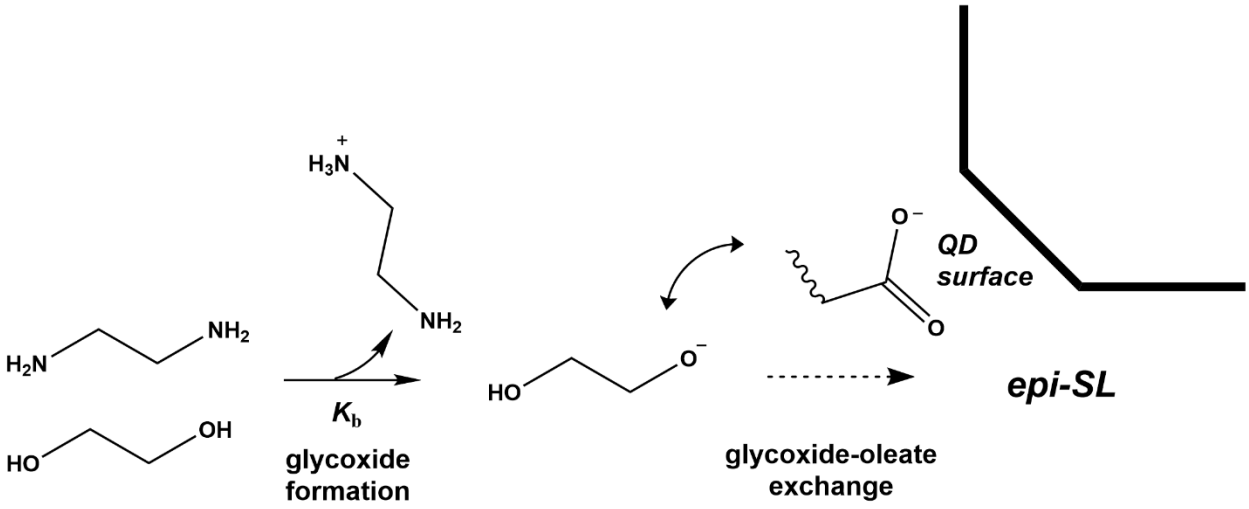

Figure 1.4: *Schematic of the glycoxide-oleate exchange mechanism resulting in epi-fusion of neighboring QDs and overall epi-SL formation.*

Analysis of oleate content in QD films occurs mainly by work-up of the Fourier-transform infrared (FTIR) spectrum. Molecular bonds will vibrate in various ways if they absorb a certain energy or frequency of light. Thus, molecular structures can be identified depending on which frequencies they absorb, and to what intensity (for example, C-H alkane bonds in oleate have a distinctive three-peak pattern in the ~3200 – 2700 cm^{-1} region that will be a focus of discussion in Chapter 2). FTIR spectroscopy is an efficient way to gather a sample's spectral fingerprint, because

one scan can capture intensities at every frequency in the defined range (as opposed to measuring an intensity at each frequency individually). The fundamental component of an FTIR spectrometer is an IR source that is split into two equivalent beams:

Beam 1 is transmitted through the sample, losing some intensity as its energies are absorbed by various vibrational modes in the molecules, and is then reflected off a stationary mirror towards the detector.

Beam 2 hits a moving mirror instead of the stationary one, thus giving it a longer path length than that of Beam 1 by the time it also reaches the detector. Recombining the beams will result in some combination of destructive and constructive interference depending on the difference in path length.

Because the mirror that reflects Beam 2 is constantly moving, the resulting intensities will fluctuate like a cosine wave as a function of the path length difference caused by the moving mirror. The resulting intensity vs. path length difference plot is called an interferogram and can be thought of as a function of time. A Fourier transform of the interferogram will thus produce intensity as a function of frequency instead, which can be interchanged with energy, i.e. wavenumbers (cm^{-1}). This results in a raw FTIR spectrum. Further corrections to this raw data can be made (see Chapter 6.3) to normalize the oleate content of all samples for a given film thickness, thus allowing comparisons of different epi-SL treatments and levels of epi-fusion.

1.4 CHARGE TRANSPORT IN QUANTUM DOT SOLIDS

The band gap of a QD is a direct result of its size; the smaller the QD, the larger the band gap.[1] Since the size of the QD, and thus the resulting band gap and other optoelectronic properties, can be tightly controlled by its synthesis, this feature in particular makes QDs an attractive material

to use for exploring semiconductor applications, providing the building blocks with which to fabricate materials of tunable absorption ranges.

Following a ligand exchange that allows the fusion of neighboring QDs within the three-dimensional structure, an ideal solid of monodisperse QDs would exhibit perfectly aligned individual bandgaps, as depicted in Figure 1.5. This perfect alignment, after sufficient passivation of any trap states within the band gap, should be sufficient to allow charge tunneling through the energy barriers between individual QDs. Thus, mini-bands can form across the energy landscape of the entire solid, mimicking the delocalized charge transport observed in bulk semiconductors.[19,20]

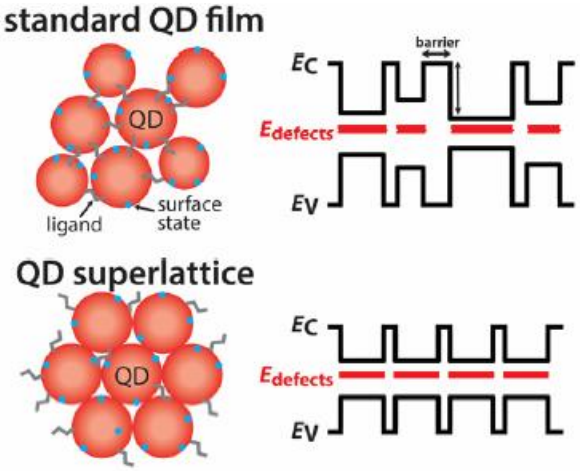

Figure 1.5: *Energy diagrams of (top) a typical QD film and (bottom) an ideal QD superlattice. In an energy diagram, negatively charged electrons can be excited from an energy state in the valence band, E_v, to an energy state the conduction band, E_c, leaving behind a positively charged hole in an E_v energy level. Typically, energy barriers between individual QDs prevent charge transport from one band to its neighbor, and charges can be trapped in a mid-gap state ($E_{defects}$), which can result from an atomic defect on the QD facet, or from any leftover ligands coordinated to its surface.*

However, in experiment, fabricated QD solids instead typically facilitate hopping charge transport, where the charges are localized and must possess an energy above some threshold in

order to thermally hop to an adjacent site.[4] This is due to combination of many factors, including some QD polydispersity – usually 3-5%, inherent in even the best synthesis protocols – and incomplete ligand removal from the QD surface; the former creates nonuniformities in band gap size and alignment, and the latter increases the number of trap states within the band gap.[19] Thus, experimentally observed charge mobilities, a measure of how fast a charge can move through a solid via an electric field, in fabricated QD solids are already disappointingly low even in monolayer films, i.e., at least 3-4 orders of magnitude below the electron mobility of Si of ~1000 $cm^2V^{-1}s^{-1}$ without the use of additional surface passivation treatments or electrolytic gating.[21,22] Meanwhile, the overarching final objective of this project seeks to increase charge mobility via atomic layer deposition (ALD) as a surface passivation method, which will be discussed in further detail in the next section.

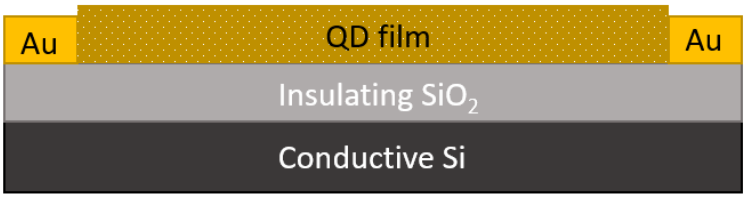

Figure 1.6: *Schematic of a typical QD FET. The gate voltage can be applied to the conductive Si layer, and the source-drain voltage can be applied, and the current collected, from across the Au electrodes on either side of the film. Typical channel lengths are 25 microns between the electrodes.*

A common method to measure charge mobility is through a field effect transistor (FET) measurement, as depicted in Figure 1.6. A FET consists of source and drain electrodes deposited on an insulating substrate a certain length apart, creating a channel between the electrodes. The channel can be gated, such that an electrical bias is applied at the bottom side of the insulating

layer of the substrate, beneath the channel. The material to be measured can then be deposited in the channel, between the electrodes and on the top side of the insulating layer.

Thus, current-voltage plots (i.e., I-V curves) of the FET device can be obtained by either applying varying source-drain voltages across the channel via the electrodes and measuring the resulting current at a constant gate voltage (i.e., an output curve), or by applying varying gate voltages and measuring the resulting current at a constant source-drain voltage (i.e., a transfer curve). Then, using the gradual channel approximation, which assumes that the gate voltage is much greater than the source-drain voltage and that the mobility is independent of carrier density, the charge mobility can be calculated using the following:[23]

$$\mu = \frac{L}{WCV_{SD}}\left(\frac{dI_{SD}}{dV_G}\right)$$

Where μ is the mobility, L is the channel length, W is the channel width, C is the oxide capacitance per unit area, V_{SD} is the source-drain voltage, I_{SD} is the source-drain current, and V_G is the applied gate voltage. As mentioned previously, typical observed carrier mobilities for QD solids cover a wide range, from 0.001 to 20 $cm^2V^{-1}s^{-1}$. For a two-dimensional QD epi-SL, i.e. a monolayer of QDs, the carrier mobility has been as high as 24 $cm^2V^{-1}s^{-1}$, albeit with the aid of an ion gel.[24] Theoretically, ideal QD epi-SLs have been calculated to achieve mobilities on the order of 100 $cm^2V^{-1}s^{-1}$ or greater.[20]

A caveat to the FET carrier mobility measurement is that it can only accurately evaluate the charge transport in first 1-2 layers of the deposited QD film in the channel. In this regard, Hall effect measurements, which involve a Van der Pauw geometry with four electrode contacts, one at each corner of the film, and a different set of carrier mobility calculation equations, would

provide a more accurate evaluation of electrical properties for the bulk QD solid.[25] Still, FET measurements are simpler to execute and are a reliable point of comparison with at least monolayer films; bulk Hall effect measurements of the QD films described by this dissertation will be left for future studies.

1.5 ATOMIC LAYER DEPOSITION AND SURFACE PASSIVATION

QDs are air-sensitive, meaning that their practical application in devices is limited without adequate long-term passivation. Thus, many report varying degrees of success with processes that involve semiconducting polymers and halides to both passivate surface defects in the QD film as well as provide air stability.[11,16] However, one method in particular has shown great promise and has been a focus of this group's QD research: atomic layer deposition (ALD) of an inorganic material.

The ALD process involves placing the film, which can be heated to an appropriate temperature, in a vacuum chamber under constant purge of an inert gas, such as nitrogen. A volume of gaseous precursor can then be released, forming a self-terminating monolayer of molecules on the film. The excess precursor vapor is then fully removed from the chamber before the next precursor is pulsed in, forming its own self-terminating monolayer that then proceeds to react with the previous. Thus, one full cycle of ALD produces a single conformal layer of the desired inorganic on the sample. Because the precursors are gases, they can easily diffuse through the spaces in between individual QDs, infilling the film to passivate electronic defects, as well as protectively coating the outside to provide air stability once the device is exposed to the ambient atmosphere for extended periods.[14,26] Thus, the energy diagram for an ALD infilled epi-SL should look similar to Figure 1.7.

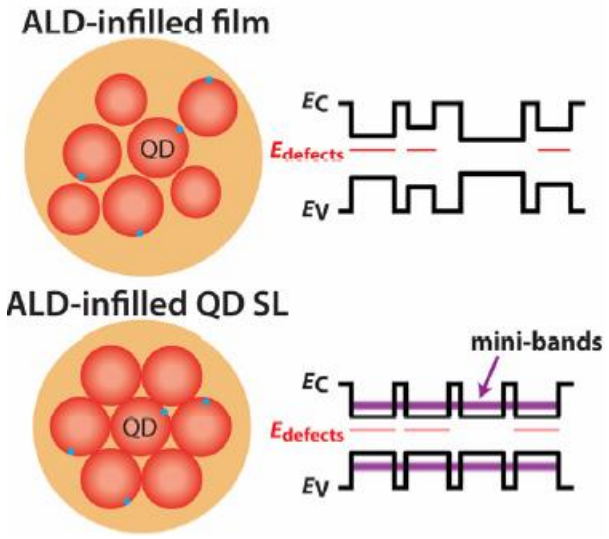

Figure 1.7: *Energy diagrams after ALD infilling of (top) an amorphous QD solid and (bottom) a QD epi-SL. ALD infilling has been shown to passivate dangling bonds from residual surface ligands as well as other atomic defects of the QD, thereby decreasing the density of trap states in the band gap. Once coupled with the monodispersity of an ideal QD epi-SL, charge carriers are now able to tunnel through the barrier between individual QDs and are less likely to land in a trap state, thus enabling delocalized charge transport throughout the entire solid.*

ALD has already been used with QD films to achieve exceptional improvement in charge transport of the resulting FET devices. Electron mobilities of thick (~300 nm), dip coated films, i.e., zero spatial order, infilled with alumina ALD have been reported to be 7 $cm^2V^{-1}s^{-1}$ or greater, indicating at least one order of magnitude higher electronic performance than the same QD film without ALD treatment.[14] Epi-SLs, on the other hand, perform slightly better than an amorphous QD SL before ALD – most probably due to the increased spatial order in the film, even with <1 micron grain sizes, and demonstrate electronic behavior associated with high doping upon ALD infilling, as seen in Figure 1.8. The origin of this doping is currently unclear – it could be any combination of process factors such as surface treatment, film cracking due to ligand exchange and/or stamp transfer of the epi-SL into the channel, or the change in film structure from

amorphous to polycrystalline. The doping has ultimately plateaued current epi-SL electron mobility measurements to the order of ~2 $cm^2V^{-1}s^{-1}$. Further investigations into this phenomenon are ongoing, but will not be a topic of further discussion in this dissertation.

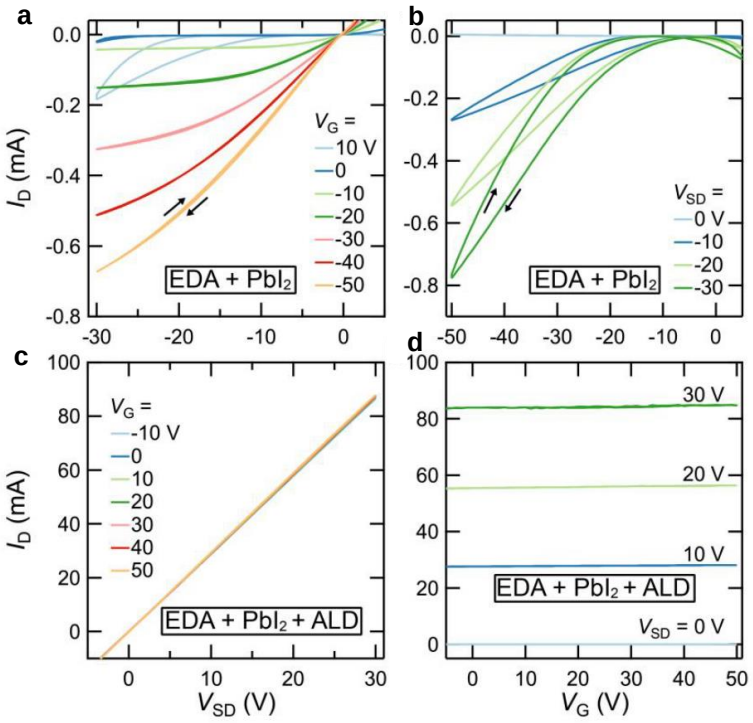

Figure 1.8: *I-V curves of epi-SLs before and after ALD. a) Output curve of an epi-SL before ALD. b) Transfer curve of an epi-SL before ALD. c) Output curve of an epi-SL after ALD. d) Transfer curve of an epi-SL after ALD. The inability to modulate the FET via the gate voltage is an indication that the epi-SL after ALD is highly doped, meaning that its carrier concentration is extremely high, and cannot be influenced by a channel bias in the device. Material from Abelson, Qian, et. al., Collective topo-epitaxy in the self-assembly of a 3D quantum dot superlattice, Nature Materials, published 2020, Springer Nature Ltd.*

CHAPTER 2 : EPITAXIALLY-FUSED, THREE-DIMENSIONAL QUANTUM DOT SUPERLATTICES

2.1 EPI-SL FORMATION BY ETHYLENEDIAMINE INJECTION

According to the method described in Chapter 6.2, the conventional method for epi-SL fabrication in regards to this dissertation has been done by point injection of ethylenediamine (EDA) into the EG subphase, at a point underneath the film such that the EDA solution is then allowed to diffuse outwards throughout the Teflon well to interact with the entire QD film. To ensure as much reproducibility as possible, the ~1.5 x 1.5 cm area of film nearest to the injection point, which is always located near the well wall and underneath the edge of the film, is transferred to the desired substrate, with the center of this transferred film being the target for chemical and structural analysis of the epi-SL according to multi-step normalization method outlined in Chapter 6.4. Analysis of the Fourier-transform infrared (FTIR) spectra of these EDA treated films concludes that this process removes ~88% of the oleate, indicated by the C-H alkane peaks 2-4, and adds a noticeable amount of glycoxide to the QD surface, as seen by peaks 7 and 8 in Figure 2.1d. An optional post-treatment is to soak the stamp-transferred epi-SL in a solution of PbI_2 in DMSO, thus removing an additional 6% of the original oleate and some of the adsorbed glycoxide.

Additionally, Figure 2.1 shows the corresponding shift from the oleate-capped, pre-EDA injection SL structure (b) to the epi-SL structure (c). In this particular example, the (100) oriented SL is depicted. Using grazing incidence small angle x-ray scattering (GISAXS) and correlated transmission electron microscopy (TEM) and electron diffraction (ED), the unit cell of the oleate capped cell was determined to be a distorted body-centered cubic lattice with an interdot distance

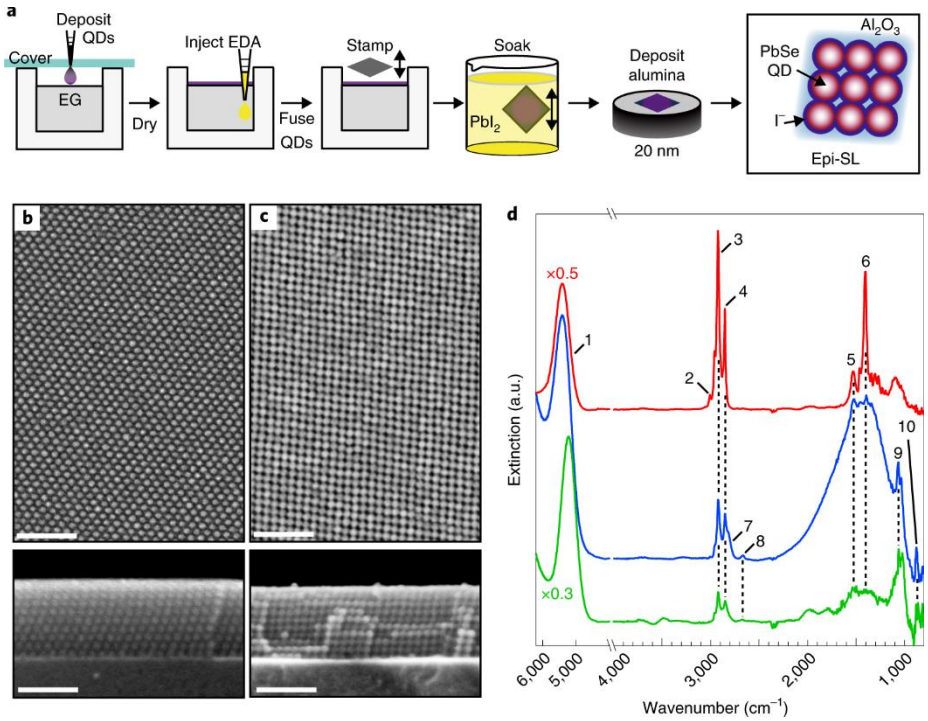

Figure 2.1: *Characterization of an epi-SL made by EDA injection. a) Process flow for the fabrication of ALD-infilled PbSe QD epi-SLs, as first seen in Figure 1.2. b) plan view and cross-sectional SEM images of a typical oleate-capped SL film on a silicon substrate, (101) SL orientation, scale bar 50 nm. c) Corresponding SEM images of an epi-SL, no ALD, (100) SL orientation, scale bar 50 nm. d) FTIR Spectra of oleate-capped (red), epi-SL after EDA treatment (blue), epi-SL after EDA and PbI_2 treatment (green). Material from Abelson, Qian, et. al., Collective topo-epitaxy in the self-assembly of a 3D quantum dot superlattice, Nature Materials, published 2020, Springer Nature Ltd.*

of 9.8 nm, oriented with either its (101) or (10-1) planes parallel to the subphase, and thus the substrate surface, with the {100} or {110} facets of the QDs, respectively, facing up, i.e., perpendicular to the surface. Upon EDA injection, the unit cell contracts and can be redefined as a distorted simple cubic lattice with an interdot distance of 6.6 nm, oriented with either its (100) or (01-1) SL planes parallel to the surface, and either the {100} or {110} QD facets, respectively, still facing up. The unit cells before and after EDA injection, i.e., oleate removal and epi-fusion, are depicted in Figure 2.2, along with schematics of how each orientation of the oleate-capped SL

transitions to its corresponding epi-SL orientation. A last alumina ALD step can be used to passivate the entire epi-SL and enhance its charge transport properties, although the intricacies of this process are being actively studied and the fine-tuning is left for the future work discussed in Chapter 5.

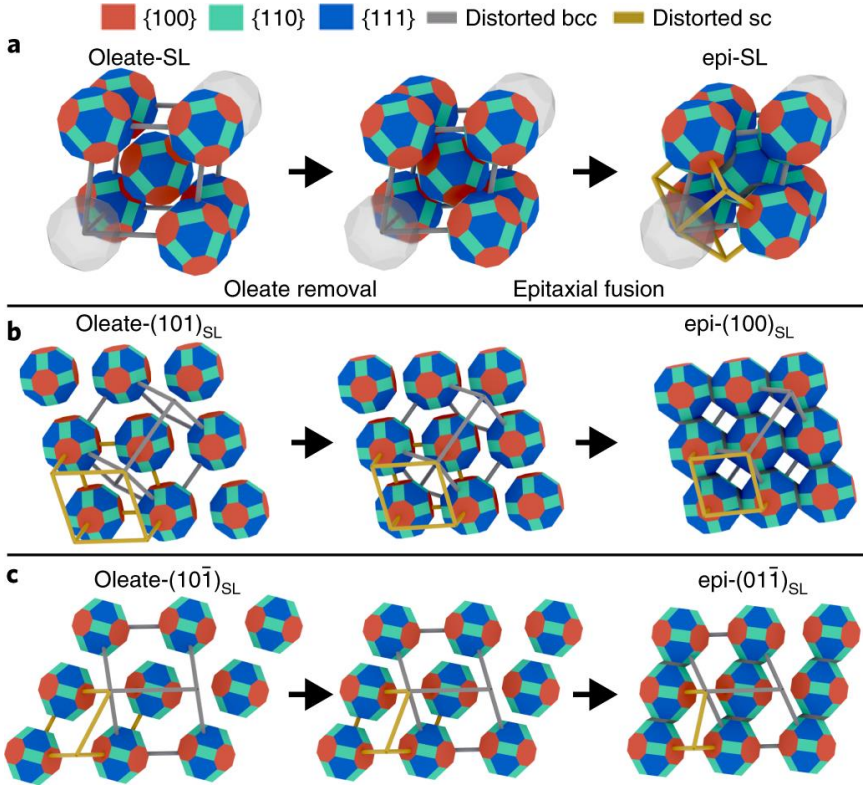

Figure 2.2: *Transformation of the oleate-capped unit cell (left) to the epi-SL (right). b) Transformation of the (101) oleate-capped SL grain to the (100) epi-SL grain. c) Transformation of the (10-1) oleate-capped SL grain to the (01-1) epi-SL grain. Material from Abelson, Qian, et. al., Collective topo-epitaxy in the self-assembly of a 3D quantum dot superlattice, Nature Materials, published 2020, Springer Nature Ltd.*

2.2 THE GLYCOXIDE-OLEATE EXCHANGE MECHANISM

Epi-SL formation via EDA injection is a process that has come to the forefront of the field in the last several years, but its mechanism remains under some contention. The adsorption of glycoxide onto the QD surface observed in the FTIR spectra of EDA-treated epi-SLs implies that the EG subphase is not completely inert during the process. Furthermore, the lack of amine adsorption to the QD surface shows that EDA may not be directly interacting with the QD surface or the oleate at all. Previously, this has been explained by a proposed chelation mechanism, wherein EDA chelates with the Pb^{2+} cation and removes both the cation and its complexed oleate from the QD surface during epi-fusion; in-depth discussion and exploration of the different ligand exchange mechanisms continues in Chapter 4.[17] However, lack of Pb^{2+} detected in the subphase after epi-SL formation indicates that this cannot be the case for QD film self-assembly on EG.[9]

To gain a better understanding of EDA's true role in the exchange process, we conducted a study of amines that vary in their pK_b values. Because pK_b is a measure of basicity, a lower value indicates that the amine is a stronger base, or more likely to accept a proton from the EG subphase, while a higher value means a weaker base, and thus less prone to accepting the proton. It should be noted that these pK_b values are reported for EG, not water, as a solvent, thus causing a slight shift in the reported equilibrium values. All EG pK_b values were found in literature except for that of EDA, which was calculated from its water pK_b value via a best-fit line relating an amine's pK_b in water to its pK_b in EG.

For the same amine concentration in the EG subphase after injection and after the same amount of treatment time, the oleate removal and epi-SL formation results are reported in Figure 2.3. The amines studied in order of increasing pK_b are piperidine, $(CH_2)_5NH$; EDA, $H_2N(CH)_2NH$; triethylamine, $N(CH_2CH_3)_3$; triethanolamine, $N(CH_2CH_2OH)_3$; aniline, $C_6H_5NH_2$; and quinoline, C_9H_7N. Figure 2.3b-c show decreasing C-H alkane peaks in the FTIR spectra of the resulting epi-

SLs with decreasing pK_b, and increasing adsorption of glycoxide, and d shows a similar relationship between pK_b and the shift to the epi-SL crystal structure. Specifically, piperidine, the strongest base in the series (pK_b = 3.7), removed the most oleate (96%) and produced moderately fused, high-quality epi-SLs. Triethylamine (pK_b = 4.5) and EDA (pK_b = 4.7) removed 67% and 89% of the oleate, respectively, and produced highly fused epi-SLs. FTIR spectra of these three types of films show the presence of adsorbed glycoxide and the absence of adsorbed amine, features consistent with glycoxide–oleate exchange. In contrast, the weaker bases triethanolamine (pK_b = 6.3), aniline (pK_b = 9.5), and quinoline (pK_b = 10.2) resulted in no oleate removal, epi-SL conversion, or glycoxide adsorption. More extreme treatments with these weaker bases (higher concentrations, longer times) may cause substantial oleate removal and epi-fusion, as was recently reported for aniline treatments of monolayer QD films. Other factors besides amine pK_b in EG, such as amine type (primary, secondary, or tertiary), denticity, and size, were not obviously correlated with oleate removal and epi-fusion. Thus, it can be concluded that amines trigger epi-SL conversion indirectly by producing glycoxide that exchanges with oleate on the QD surface.

As mentioned previously, different exchange mechanisms may be favored depending on the solvent environment. For example, prior work has shown that amines complex with and remove Pb oleate from the surface of PbX QDs in aprotic solvents (benzene, toluene).[17] In aprotic solvents, complexation with Pb oleate (the “Lewis mechanism”) is perhaps the only mechanism available for oleate removal by amines. However, another mechanism becomes possible in protic solvents such as EG: the amines can deprotonate the solvent and the deprotonated solvent anions can directly exchange with oleate, without Pb removal (the “Brønsted mechanism”). Under the

current experimental conditions, EDA should be a better complexing agent than the other amines in this study because it is a bidentate ligand and one of the strongest Lewis bases among these amines, but EDA shows no Pb^{2+} removal. Given the chemical similarity of EDA to the other amines studied here, it is very unlikely that the other amines would show appreciable complexation

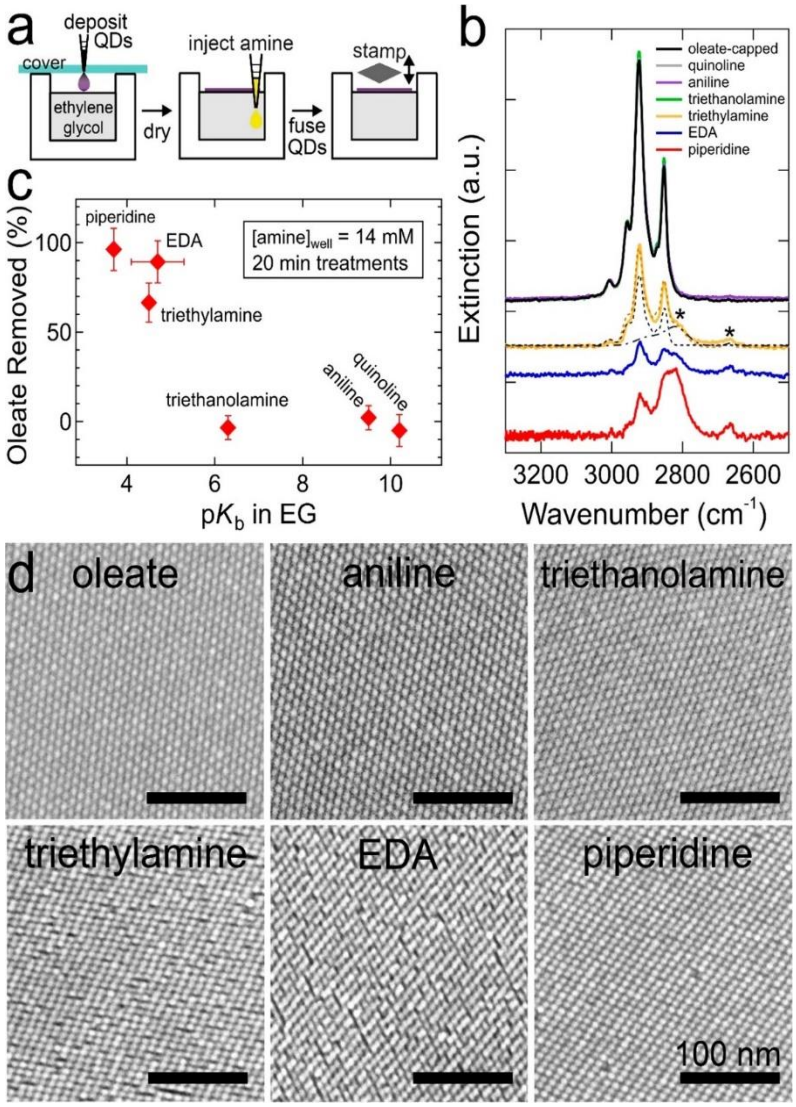

Figure 2.3: *Amine injection study. a) Cartoon of the fabrication process. b) Typical FTIR spectra of an oleate-capped SL, aged on EG by 20 min, and SLs treated by one of six different amines, total amine concentration of 14 mM and 20 min treatment time. c) Plot of the percent oleate removed versus pK_b of each amine in EG. d) Representative plan view SEM images of the oleate-capped film and films treated with 5 of the 6 amines (quinoline omitted because of similarity to aniline and triethanolamine).*

and stripping of Pb when EDA shows none. Nevertheless, it is possible that both the Lewis and Brønsted mechanisms may be simultaneously active and important for some protic solvent/amine pairs, and it may be the case that some amines remove some amount of Pb even in EG.

If glycoxide–oleate exchange is indeed the chemical mechanism that triggers epi-SL formation, then replacing the amine with a non-amine base that generates sufficient glycoxide should also produce the epi-SL. Thus, it follows that the simplest base, hydroxide ion (OH^-), should also be able to perform similarly to the low pK_b amines. Our next set of experiments utilized different concentrations of tetrabutylammonium hydroxide (TBAOH) injected into the EG subphase in the same way as the amine study was performed. TBAOH was selected because it is reasonably soluble in EG and delivers a cation with no complicating acid/base properties or affinity for the QD surface. TBAOH is expected to quantitatively deprotonate EG, such that [glycoxide] = $[TBAOH]_0$.

As seen in Figure 2.4, the hydroxide-treated and amine-treated films have nearly identical FTIR spectra and SEM images for the same effective glycoxide concentration. As with the amine treatments, the FTIR spectra of films treated with hydroxide depicted in Figure 2.4a show loss of oleate, the presence of adsorbed glycoxide, and no evidence for adsorption of the treatment molecule itself. The degree of both oleate removal and epi-fusion increased with increasing initial TBAOH concentration ($[TBAOH]_0$) from 0 to 600 μM, as seen in Figure 2.4b-c. Oleate removal shows a sigmoidal dependence on $[TBAOH]_0$, increasing rapidly from ~8% at $[TBAOH]_0$ = 100 μM and then slowing to ~83% at $[TBAOH]_0$ = 600 μM. Recasting $[TBAOH]_0$ in terms of [glycoxide] permits a direct comparison with the oleate removed by the amines, for which [glycoxide] is readily calculated from the amine concentration and pK_b value in EG. The data are

in good agreement, suggesting that the amount of oleate removed from the QD films is largely determined by the glycoxide dose generated from the injected base (either TBAOH or amine).

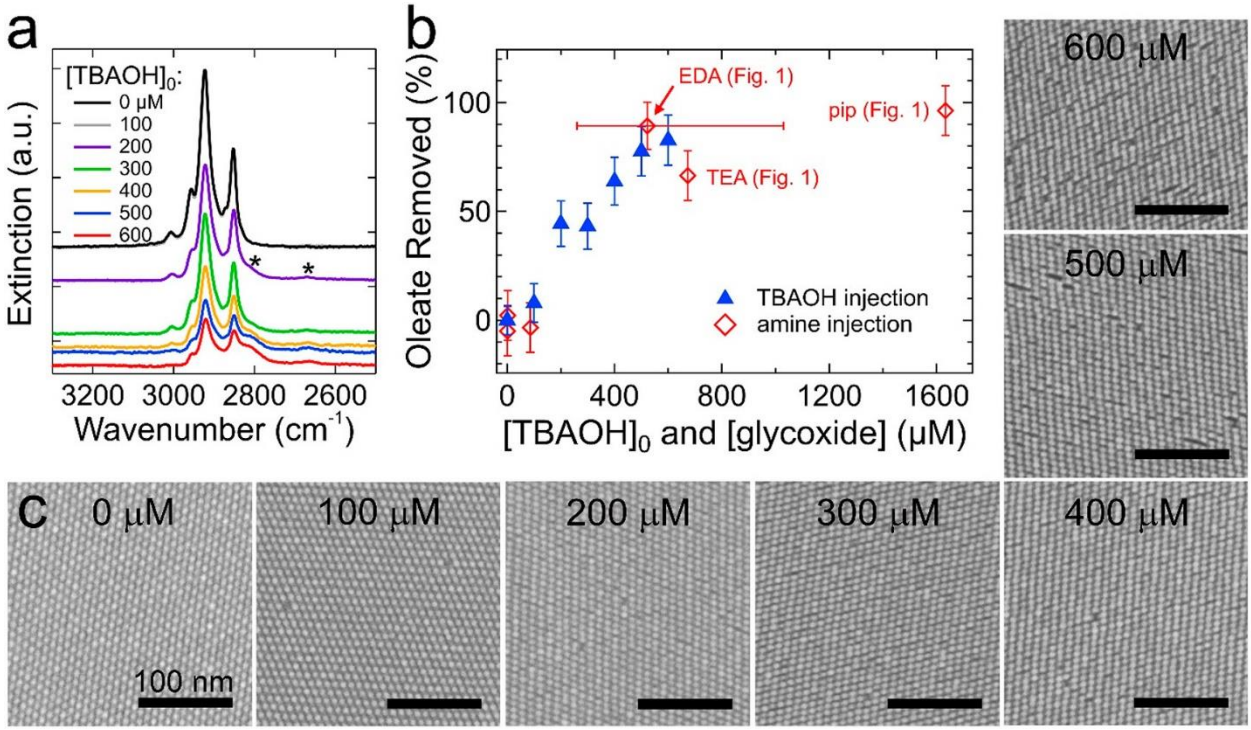

Figure 2.4: *TBAOH injection study. a) Typical FTIR spectra of an as-made oleate-capped film and films treated with 100–600 μM of TBAOH for 20 min; the characteristic shoulder and small low-energy peak of adsorbed glycoxide are labeled with asterisks. b) Plot of the percent oleate removed versus the initial total concentration of TBAOH in the quartz dish, overlaid with the data for the films made by amine injection from* Figure 2.3*; TEA = triethylamine, pip = piperidine. c) Representative plan-view SEM images of the hydroxide-made films.*

Meanwhile, the SEM image series shows that the oleate-capped SL converts to the epi-SL when $[TBAOH]_0 \geq 200$ μM. Epi-SLs made at intermediate $[TBAOH]_0$ appear to have the best structural order, while the QDs are somewhat overfused and the films more defective at the higher TBAOH concentrations (≥500 μM). These results demonstrate that amines are not needed for epi-SL formation and suggest that any base that produces a sufficient amount of glycoxide can trigger the epi-SL transformation on EG. In general, a base added to a protic solvent such as EG is

expected to produce some concentration of deprotonated solvent anions that can act as X-type ligands to replace oleate. Indeed, it is likely that many anions other than glycoxide (e.g. thiocyanate, halides, carboxylates) can exchange with oleate to produce high-quality epi-SLs, or for Brønsted–Lowry acids (e.g. carboxylic acids, alkylammonium iodides) to protonate and remove oleate as oleic acid and replace it with the attendant anion (carboxylate, iodide); both of these possibilities will be discussed in Chapter 4. The main requirement for glycoxide-oleate exchange seems to be that the supplied anion displaces oleate while the cation forms an oleate salt that is sufficiently soluble in EG.[27,28] Thus, there are both basic and acidic routes to oleate ligand exchange and epi-SL formation.

2.3 TOWARDS MORE UNIFORM LIGAND EXCHANGE

While the injection of a chemical trigger to initiate QD film ligand exchange has been the conventional method for producing epi-SLs, this process has inherent disadvantages. First, there is an extreme diffusion gradient from the point of injection laterally throughout the subphase, meaning that the area of film closest to the injection point will be exposed to a much higher dose of chemical trigger, and thus a much higher [glycoxide], than observed at an area on the opposite side of the film. This radial concentration gradient of glycoxide under the QD film results in laterally nonuniform degrees of ligand exchange and epi-fusion.

Additionally, introducing a separate volume of solution into the subphase, no matter how controlled the manner of injection, will cause some turbulence beneath where the film is floating, leading to excessive cracking of the film beyond what is a byproduct of film contraction upon ligand exchange. ultimately, the vibration, surface waves, convective liquid currents, vortices, and

other mechanical disturbances produced by point injection are all effects that can damage the delicate floating QD film.

Approaches taken to remedy these issues attempt to distribute the chemical trigger more uniformly throughout the subphase. For example, the "showerhead" design depicted in Figure 2.5. The well consists of two halves that can be threaded together to make one complete piece, wherein the chemical trigger is injected through a side port on the bottom half and released into the space beneath the showerhead via the center opening, after which it can then diffuse upwards through the showerhead holes. The top half is the well itself, with lines of holes extending outwards radially from the center of the well floor. The holes are sized such that those located farther from the center also have a larger radius, such that when the chemical trigger exits the center opening, larger doses

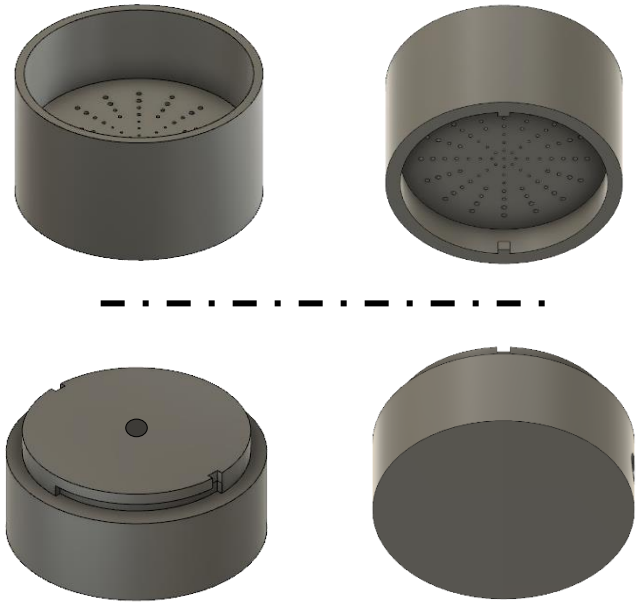

Figure 2.5: *Schematic of the "showerhead" Teflon well. On the bottom half, the injection port is partially visible on the right side; a path is subsequently bored through the Teflon until it reaches the center, where it meets the pathway drilled down from the center opening. Note that upon actual fabrication of the well, the depicted threading mechanism was replaced with NPT threading machined into the Teflon.*

of the chemical trigger will be released to the outer edges of the film to compensate for the larger distance from the "point" of injection.

While showing promise, the "showerhead" design fails to completely remove the turbulence-associated mechanical damage of the film inherent to an injection method, although the effects are greatly reduced through use of a separate chamber of EG underneath the showerhead that absorbs the bulk of the injection force before the injected chemical trigger and/or produced glycoxide is allowed to diffuse upwards through the showerhead to remove oleate from the film. In addition, the desire for a simpler method of uniform ligand exchange is still apparent.

To remove the turbulence effect of the injection method, the chemical trigger must be already present in the EG subphase prior to self-assembly of the QD film, and yet remain inert until after the oleate-capped SL has dried. It is reasonable to ask if similar ends could be achieved more easily by simply dissolving a conventional base (e.g. an amine or hydroxide) in the EG before depositing the QD suspension on the EG surface. This approach might also yield laterally uniform, contactless ligand exchange while avoiding the added complexity of photochemical triggering. However, casting the QD dispersion onto EG that already contains a significant amount of base (and thus glycoxide) results in poor-quality, nearly amorphous films because self-assembly and ligand exchange occur simultaneously rather than sequentially. The glycoxide generated by the base begins to strip oleate from the QDs as soon as the two solutions make contact, ruining SL formation. Thus, self-assembly and ligand exchange must be separated in time to make good films; it is essential to first assemble a high-quality oleate-capped SL and then trigger epi-SL conversion with base addition. The possibility of layering solvents, such that the chemical trigger is present only in the bottommost layer and must diffuse through a sufficient "buffer" layer of pure EG in the time it takes the oleate-capped SL to self-assemble and dry, was also explored, but the height

of the buffer layer required to sufficiently separate the glycoxide from the still assembling oleate-capped film is too large to be practical.

The most promising method to date features a much simpler experimental design than the "showerhead" or solvent layering approaches. It utilizes a photobase generator (PBG) that is pre-dissolved in the EG subphase before the deposition of any QD solution, allowing the oleate-capped film to finish assembling before the PBG is activated via UV light to release the appropriate chemical trigger, as highlighted in the next section.

2.4 EPI-SL FORMATION BY PHOTO-TRIGGERED BASE RELEASE

In the photobase approach, an oleate-capped SL is assembled on an evenly mixed solution of PBG in EG. The PBG molecule itself is a very weak base (high pK_b) that does not cause QD fusion or otherwise affect the oleate-capped SL. However, when illuminated with light of the proper wavelength, the PBG releases a stronger base (lower pK_b) that produces sufficient glycoxide to trigger epi-SL conversion. The PBG (*E*)-1-piperidino-3-(2-hydroxyphenyl)-2-propen-1-one (commercially referred to as WPBG-027), undergoes photochemical cleavage to release piperidine (pK_b = 3.7 in EG) when illuminated with UV light, as depicted in Figure 2.6b. Photobase illumination promises to yield films with better structural–chemical uniformity, less mechanical damage, and better control of the glycoxide dose than conventional point injection. In contrast to point injection, illumination of a PBG dissolved in the subphase should produce a uniform glycoxide concentration in the plane of the film, enabling laterally uniform ligand exchange and QD fusion across the entire epi-SL. The photobase method is also contactless and gentle and avoids mechanical damage. Furthermore, it provides a convenient way to control the

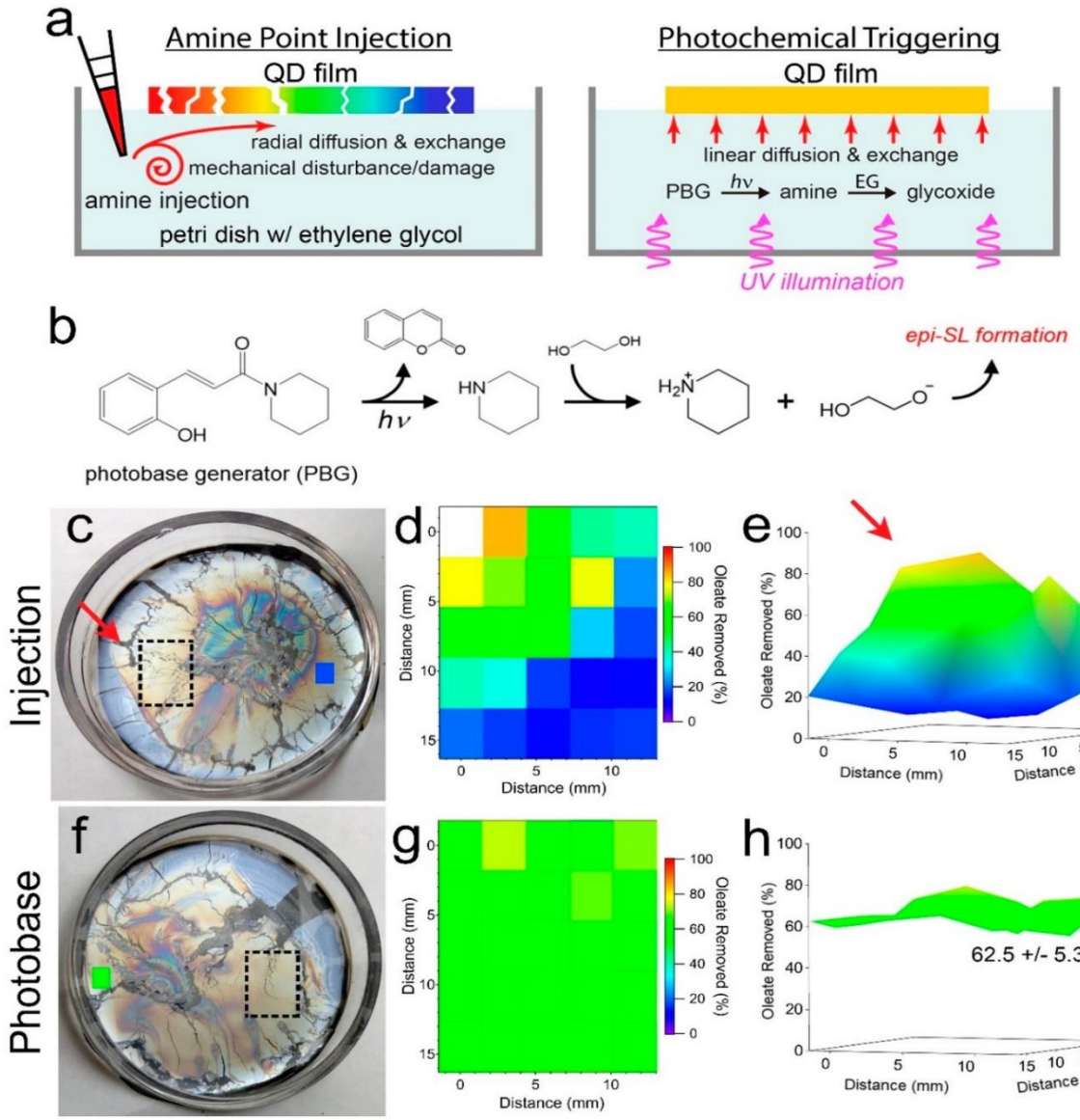

Figure 2.6: *The photobase epi-SL fabrication method. a) Schematic depictions of the conventional point injection method (left) compared to the photobase method (right); the color of the QD films denotes the degree of local oleate removal. b) Proposed reaction cascade for photochemically triggered epi-SL conversion. c) A floating oleate-capped SL film prior to piperidine injection; the red arrow indicates the location of piperidine injection. d) 2D map of the percent oleate removed from the film. e) 3D view of the map f) Photograph of the floating film before illumination. g) 2D map of the percent oleate removed. h) 3D view of the map.*

glycoxide dose (concentration–time profile) by adjusting the illumination intensity and time, allowing for the fabrication of more perfect epi-SLs by fine-tuning the kinetics of ligand exchange

and epi-fusion.

The presented PBG study focuses on the first two advantages (better film uniformity and reduced mechanical damage); the investigation into the importance of improved glycoxide dose control will be discussed as part of the future work summarized in Chapter 5.

FTIR and SEM mapping were used to compare the lateral chemical and structural uniformity of films made by amine point injection and photobase illumination. Figure 2.6c shows a photograph of a floating oleate-capped SL film prior to piperidine injection. A solution of piperidine in EG was carefully injected into the subphase near the edge of the film (red arrow) and allowed to diffuse and exchange with the film for one hour, at which time the film was stamped onto a silicon substrate for analysis. A 1.5 × 1.2 cm region of the film close to the injection point was mapped by FTIR spectroscopy (5 × 5 array, dashed rectangle outlined in Figure 2.6c). The resulting map of oleate removal shows a pronounced radial gradient, as expected, with oleate loss decreasing from ~85% closest to the injection point to only ~15% farthest from the injection point, as seen in Figure 2.6d-e. While mapping the entire QD film was not entirely possible due to the large film size, one additional point at the far side of the floating film (blue rectangle in Figure 2.6c) was measured to have an oleate loss of 17%, which is consistent with a fairly steep ligand exchange gradient around the injection point and relatively little oleate removal (10–20%) across most of the film. In fact, as a function of distance from the injection point, oleate removal decreases rapidly and falls below 20% at ~1.5 cm from the injection location, as depicted in Figure 2.7.

SEM images collected at the 25 FTIR spots were used to make corresponding maps of inter-QD distance, film densification, and area per QD. These three parameters exhibit radial gradients similar to that of oleate removal. Visual inspection of the SEM images shows that the degree of epi-fusion decreases with radial distance and that no epi-fusion occurs beyond ~1.7 cm

from the injection point. There is also a strong inverse dependence of the inter-QD distance on oleate removal and an apparent threshold of >25% oleate removal for conversion of the oleate-capped SL to the epi-SL, as seen in Figure 2.7. Overall, it is clear that point injection produces highly inhomogeneous films with strong lateral gradients in ligand coverage, inter-QD distance, and epi-fusion.

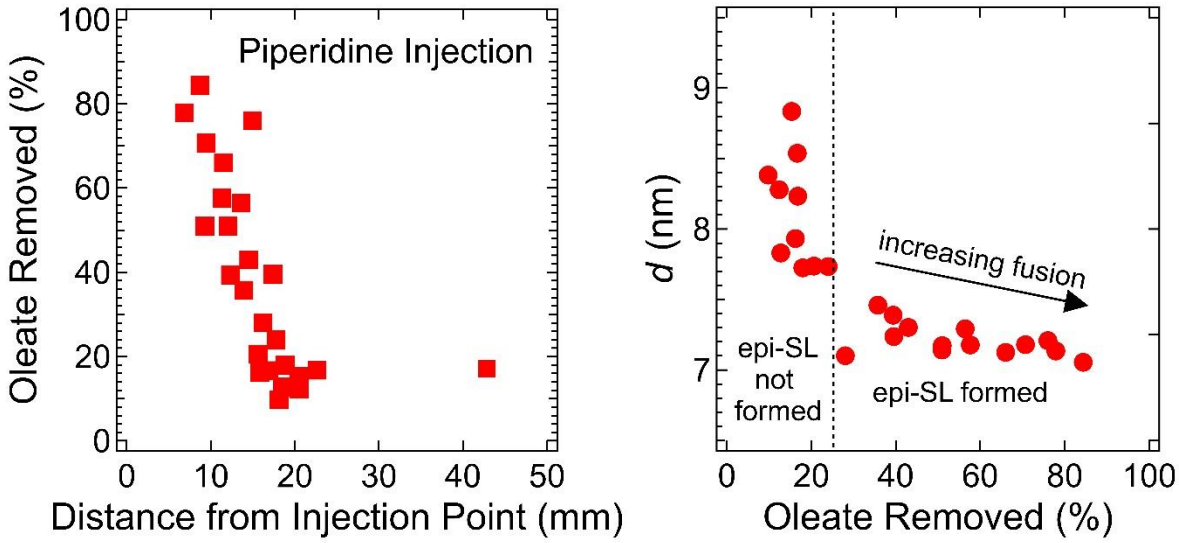

Figure 2.7: *(left) Oleate removal versus distance from the point of piperidine injection, from data reported in Figure 2.6. (right) Inter-QD distance versus oleate removal for the same film made by piperidine injection.*

In contrast to films made by piperidine injection, films made by photobase illumination are very homogeneous, with uniform oleate removal, inter-QD distance, and epi-fusion across the entire film surface. Figure 2.6f shows a photograph of a floating oleate-capped SL film prior to illumination. The EG subphase contained 1 mM of the PBG. The film was then illuminated from below with 254 nm light from a mercury lamp (1.5 mW cm^{-2}) for one hour and exchanged for another 4 hours in the dark before being stamped onto silicon. The map of oleate removal in Figure 2.6g-h shows a uniform value of 62.5 ± 5.3%. The point on the far side of the film (green rectangle in Figure 2.6f) had an oleate loss of 57%, demonstrating uniformity across the entire film. The

maps of inter-QD distance, film densification, and area per QD are similarly uniform, with values of 7.25 ± 0.11 nm, 13.8 ± 2.7%, and 67 ± 2 nm^2/QD, respectively. These narrow distributions reflect the inherent lateral uniformity of photobase-triggered epi-SL conversion. FTIR spectra of the photobase-made films were indistinguishable from spectra of films made by piperidine injection, with both showing adsorbed glycoxide but no adsorbed piperidine, which is again consistent with glycoxide–oleate exchange.

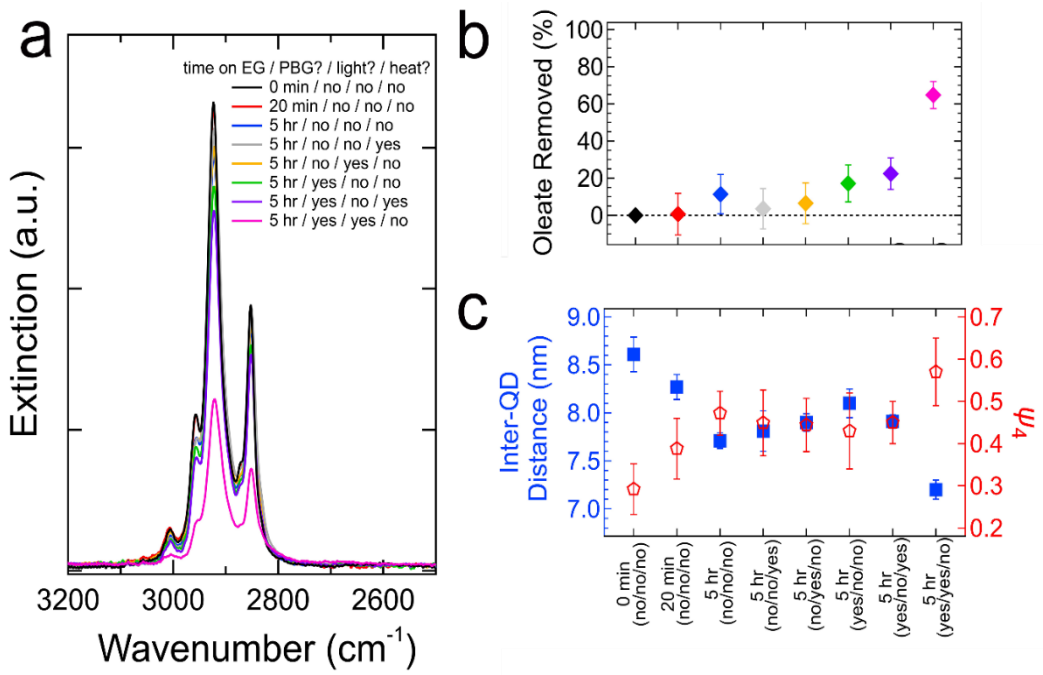

Figure 2.8: *PBG control experiments. a) Baseline-corrected FTIR spectra of films treated with different combinations of PBG, UV illumination, and heating. Samples are labeled with their total time floating on EG and whether the sub-phase contained PBG, whether the sample was illuminated with 254 nm light, and whether the sample was heated on a hotplate to 38 ºC. b) Percent oleate removal for the control samples and the normal photobase-made epi-SL. c) Inter-QD distance and* Ψ_4 *values for the control samples and the normal photobase-made epi-SL.*

Control experiments confirmed that photochemically triggered epi-SL conversion requires both the PBG and UV illumination. Films illuminated in the absence of PBG showed minimal

oleate loss (<10%) and no epi-fusion, as seen in Figure 2.8a-b. Films exposed to PBG without UV light had somewhat higher oleate removal (~15%) but no epi-fusion. Since the UV lamp also slightly warms the samples (to 37–38 °C), additional control experiments in which floating films were aged on a hot plate at 38 °C without UV illumination were also completed. Samples heated without PBG had <10% oleate loss and no epi-fusion, while samples heated with PBG showed ~22% oleate loss, but again the epi-SL did not form. Only PBG together with UV illumination resulted in major oleate loss (~65%) and formation of the epi-SL. These control experiments demonstrate that epi-SL conversion is caused by the proposed photochemistry rather than an alternative mechanism such as dark aging of the QD film by EG or the PBG, film heating, or direct excitation of the film by UV light.

2.5 STRUCTURAL CHARACTERIZATION OF QUANTUM DOT SOLIDS

In addition to manual analysis of SEM FFTs to calculate parameters such as the in-plane inter-QD distance (*d*, nm) and QD number density (QDs/nm^2) to characterize the degree of oleate-to epi-SL conversion, we quantitatively analyzed SEM images via machine learning (ML), extracting the metrics of *d* and QD number density of the amine- and hydroxide-treated films, as well as the additional parameter of SL symmetry. Figure 2.9 shows the ML-analyzed *d*, the center-to-center distance between neighboring QDs along the [100] superlattice direction, and the squareness parameter Ψ_4, which provides a local measure of the degree of 4-fold symmetry of the SL.[29]

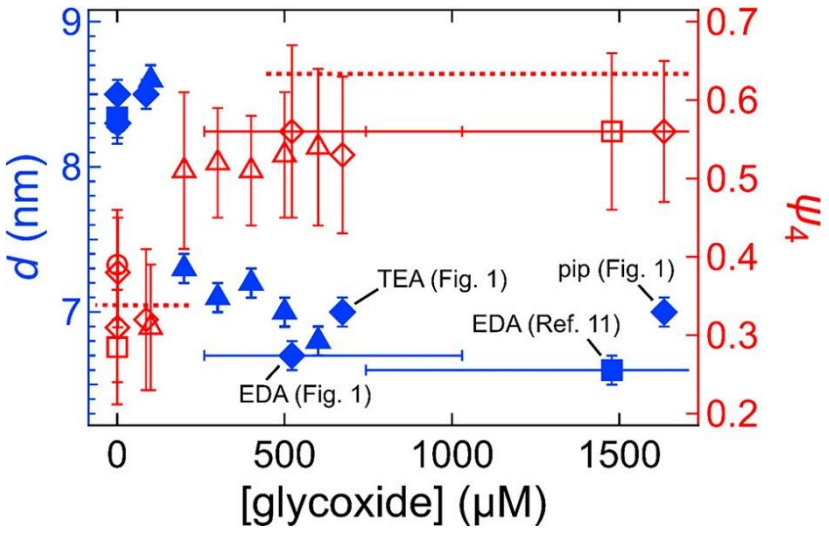

Figure 2.9: *Lateral inter-QD distance and superlattice squareness parameter for the amine- and hydroxide-treated films. Diamonds and triangles are the amine-treated films and TBAOH-treated films, respectively. Circles are an oleate-capped film aged for 20 min on EG. Squares are the oleate-capped and EDA-treated films reported in Abelson et. al. The QDs used in ref 13 had an idealized spherical diameter of 6.5 nm, compared to 6.9 nm in the current work; horizontal red dashed lines are calculated Ψ_4 values for the unit cells of the oleate-capped SL and epi-SL in Abelson et. al.*

For these films, we observe a sudden change in both parameters at a threshold glycoxide concentration of ~200 μM. The average inter-QD distance decreases from 8.3−8.6 nm for [glycoxide] ≤ 100 μM to 6.7–7.3 nm for [glycoxide] ≥ 200 μM, with the EDA and 600 μM TBAOH treatments resulting in the smallest average distances (6.7 and 6.8 nm, respectively, just 1–2 Å larger than the diameter of these truncated cuboctahedral QDs in the ⟨100⟩ directions). The inter-QD distance also decreases slightly from 7.3 to 6.8 nm with increasing TBAOH concentration from 200 to 600 μM. Meanwhile, Ψ_4 jumps from 0.29−0.39 for [glycoxide] ≤ 100 μM to 0.51–0.56 for [glycoxide] ≥ 200 μM. The step-like change in these two parameters indicates that the epi-SL phase transition occurs abruptly over a narrow range of [glycoxide]. Sufficient oleate exchange with glycoxide enables strong inter-QD interactions that lead to a sudden change in local SL

symmetry and concurrent densification of the SL. As the interdot distance shrinks, the QDs "click" together, forming a rigid distorted simple cubic lattice with the QDs fused along their {100} facets. Additional fusion leads to only a small additional decrease in the inter-QD distance as the necks thicken and shorten.

The d and Ψ_4 values of the photobase film samples reveal that contact with EG itself causes moderate densification and structural evolution of the floating QD films. For all of the control samples (5 hours on EG), d = 7.7–8.0 nm and Ψ_4 = 0.43–0.47, compared to d = 8.6 nm and Ψ_4 = 0.29 for the oleate-capped SLs and d = 7.2 nm and Ψ_4 = 0.57 for the epi-SLs made by photobase illumination (Figure 2.8c). We speculate that wetting of the films by EG increases oleate interdigitation, compaction, and/or diffusion on the QD surface, resulting in the observed density and squareness increase despite the small amount of oleate removed from these samples. In fact, even films aged for only 20 min on pure EG — for which oleate loss was negligible — showed significant changes in d and Ψ_4 (d = 8.3 nm and Ψ_4 = 0.39). Table 2.1 highlights the relationship between the different glycoxide concentrations of the reported amine, TBAOH, and photobase treatments and the resulting oleate removal reported previously in this chapter.

SEM imaging was also used to compare the morphologies and structural defect concentrations of the photobase-made and injection-made films. Films made as per Figure 2.6 were imaged in many different locations at both "high" and "low" magnification. The photobase-made films, which are laterally uniform, were imaged at randomly selected spots across their entire surfaces, while the injection-made films were imaged at randomly selected spots within the small region of each film that had values of oleate removal, inter-QD spacing, and Ψ_4 equivalent to those of the photobase-made films.

Chemical / EG pK_b	Treatment / concentration	[glycoxide] (μM)	Oleate removal (%)
Piperidine / 3.7	Injection, 20 min / 14 mM	1600	96
EDA / 4.7	Injection, 20 min / 14 mM	510	89
EDA v3.0 / 4.7	Injection, 30 sec / 106 mM	1400	80
Triethylamine / 4.5	Injection, 20 min / 14 mM	640	66
Piperidine / 3.7	Injection, 1 hr / 1 mM	360	65
Piperidine / 3.7	PBG / 1 mM	360	63
Triethanolamine / 6.3	Injection, 20 min / 14 mM	82	0
Aniline / 9.5	Injection, 20 min / 14 mM	2.1	0
Quinoline / 10.2	Injection, 20 min / 14 mM	0.93	0
TBAOH	Injection, 20 min / 600 uM	600	83
	Injection, 20 min / 500 uM	500	78
	Injection, 20 min / 400 uM	400	64
	Injection, 20 min / 300 uM	300	43
	Injection, 20 min / 200 uM	200	44
	Injection, 20 min / 100 uM	100	8

Table 2.1: *Glycoxide concentration and % oleate removal of all reported epi-SL fabrication methods.*

Figure 2.10 presents representative images of both types of films. The high-magnification images (a and c) show that the injection-made films have a much higher concentration of nanoscale extended defects. Some of these defects are relatively large nanoscale tears/rips in the films, highlighted with the red ovals. Such features are defined as “nanotears” if they have a short

dimension of 5–25 nm. In addition to nanotears, the injection-made films also contain a large number of thinner (<5 nm) parallel tears that cut across the QD chains of the (01-1) superlattice grains, splitting the QD chains into shorter segments, as outlined by the blue oval in Figure 2.10. These defects are rows of missing necks between QDs. We classify these defects as "chain splits" if they are at least three QDs long. Chain splits are ubiquitous in the injection-made films but rare in the photobase-made films.

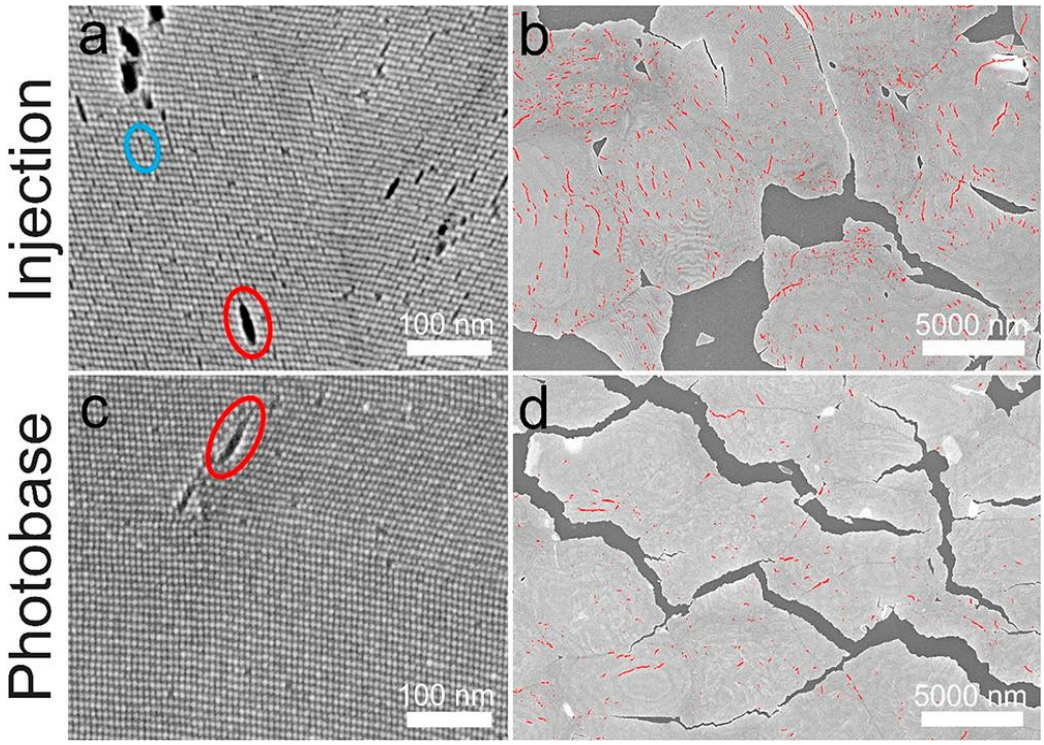

Figure 2.10: *Defect distributions for the two epi-SL fabrication methods. a) Representative high-magnification image of an epi-SL film made by piperidine injection, showing a high density of nanoscale tears (e.g. red oval) and* $[100]_{SL}$ *chain splits (e.g. blue oval). b) Representative low-magnification image of an injection-made film, showing a high density of intraflake cracks (shaded red). Interflake cracks are unshaded. c, d) Corresponding representative images of photobase-made epi-SLs, showing the absence of chain splits and significantly lower density of nanotears and cracks (shaded red in d).*

Manual quantitative analysis of over two dozen images was performed to determine the typical concentration of nanotears and chain splits in the two types of films. We find a nanotear density of 29 ± 12 μm^{-2} in the injection-made films versus 6 ± 6 μm^{-2} in the photobase-made films, while the density of chain splits is 68 ± 23 and 4 ± 4 μm^{-2}, respectively. The photobase-made films have much lower densities of nanotears and chain splits. Table 2.2 summarizes these statistics. We also found high concentrations of nanotears and chain splits in injection-made films that had more oleate (only 40–50% oleate removal) and a larger inter-QD distance (7.2–7.4 nm) than the photobase-made films, demonstrating that high defect densities are a robust characteristic of the injection-made films and not the result of excessive QD fusion or small sample-to-sample differences in oleate content or inter-QD distance.

	Injection-made epi-SLs	**Photobase-made epi-SLs**
Oleate removed	59 ± 9%	54 ± 9%
d	7.1 ± 0.1 nm	7.2 ± 0.1 nm
Ψ_4	0.552 ± 0.089	0.565 ± 0.085
Nanotear density	29 ± 12 μm^{-2}	6 ± 6 μm^{-2}
Chain split density	68 ± 23 μm^{-2}	4 ± 4 μm^{-2}
Crack density	4.9 ± 1.2 μm^{-2}	0.79 ± 0.21 μm^{-2}
Crack area	2.4 ± 0.33% of film	0.63 ± 0.22% of film

Table 2.2: *Statistical comparisons of defects in injection-made and photobase-made epi-SLs.*

While the high-magnification images show the small extended defects, the low-magnification images provide information about the morphology and distribution of the bigger defects, particularly cracks within individual flakes in a film (intraflake cracks, shaded red in

Figure 2.10) and between adjacent flakes in a film (interflake cracks). Representative low-mag images (Figure 2.10b,d) demonstrate that the photobase-made films have fewer and smaller intraflake cracks than the injection-made films. Note that in these low-mag images the chain splits and smaller nanotears are not visible and many of the closely spaced nanotears appear as single continuous cracks, so the cracks are undercounted. Analysis of five images of each film type reveals an intraflake crack density of $4.9 \pm 1.2\ \mu m^{-2}$ in the injection-made films and only $0.79 \pm 0.21\ \mu m^{-2}$ in the photobase-made films. These cracks account for $2.4 \pm 0.33\%$ and $0.63 \pm 0.22\%$ of the total area of the flakes in the injection-made and photobase-made films, respectively. The images in Figure 2.10b and d, shaded to indicate intraflake cracking, emphasize that the injection-made films are riddled with cracks, many of which are clustered together in parts of the films, while the photobase-made films have significantly fewer cracks. The explanation for this difference is still undetermined, and possibilities are further discussed in Chapter 5.

Both the photobase-made and injection-made films have extensive interflake cracking (the unshaded cracks in Figure 2.10b,d). In general, the photobase-made epi-SLs are more continuous and their flakes are better interconnected, but the difference is small. Image quantification shows that the photobase-made films cover 91.4% of the substrate, compared with only 82.5% for the injection-made films. Some, and perhaps most, of the interflake cracks are created when the films are stamped from EG onto the Si wafer, which is itself a very violent process and probably the most intractable limitation on epi-SL film quality for current implementations of the Langmuir–Schaefer approach. Another major source of interflake cracks is volume loss and film contraction during ligand exchange and epi-fusion prior to stamping. The extent of inter- and intra-flake crack creation from epi-SL conversion depends on a number of complex and poorly understood factors,

including the size, interconnectedness, and structural perfection of the grains of the parent oleate-capped SL and the dynamics of ligand exchange and epi-fusion.

CHAPTER 3 : DYNAMICS OF QUANTUM DOT SELF-ASSEMBLY

3.1 CHOICE OF SUBPHASE

As alluded to in Chapter 1.2, the subphase on which the QD self-assembly occurs plays an important role in the subsequent QD solution spreading dynamics and subsequent QD film formation. This complex interplay is the result of many factors, including surface tension, miscibility, and the material of the surrounding environment.

Extensive work has been published regarding QD self-assembly on an ethylene glycol or diethylene glycol subphase.[7,11] Ethylene glycol (EG) is an ideal subphase candidate for this self-assembly process because of its high density, low vapor pressure, and high polarity. This allows the low density, high vapor pressure, highly nonpolar QD solution to spread across its surface, and the solvent to evaporate without mixing to leave behind a dried QD film. Other short-chain glycols, such as diethylene and tetraethylene glycol, may also work, but commercially available high-purity and "anhydrous" batches of these solvents still possess water and other contaminant content several times higher than that of anhydrous EG, leading to poorly self-assembled films.

One disadvantage of EG as a subphase is its tendency to strip oleate from the QD film on its own given enough exposure time, as seen in Figure 3.1. This phenomenon is due to the protic nature of the EG molecule, i.e., it has two H atoms, one of which can be removed to produce a negatively charged glycoxide molecule that has an affinity similar to that of the oleate molecule in terms of complexing with the Pb^{2+} cation; this is the basis for the glycoxide-oleate exchange mechanism discussed in Chapter 2. By itself, EG will exist at an equilibrium:

$$HOCHCHOH \leftrightarrow HOCHCHO^- + H^+$$

Defined by an equilibrium constant, *K*. However, because *K* is apparently very small in this case, the concentration of glycoxide, $HOCHCHO^-$, is also very small, and thus can only remove an appreciable amount of oleate from a QD film floating on its surface after >10 hours.

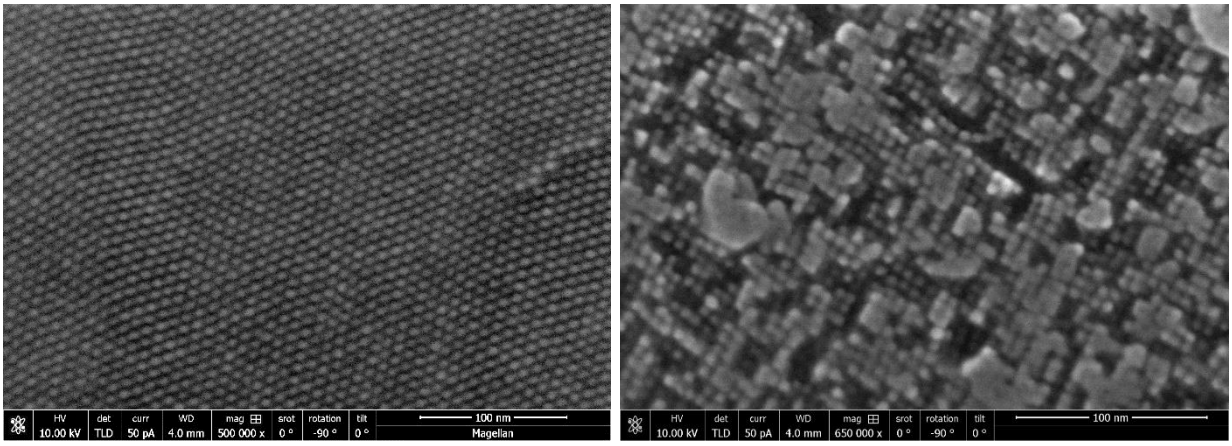

Figure 3.1: *(left) Plan view SEM image of an oleate-capped film just dried on EG. (right) Plan view SEM image of an oleate-capped film after 19 hours floating on EG.*

Thus, it would be ideal to find an appropriate subphase that not only fulfills the previously listed requirements but is also unreactive to the QD film. In this case, aprotic subphases should be explored. While there have been some reported nanoparticle self-assemblies on subphases such as acetonitrile, the complexities at the liquid-liquid interface between the QD solvent and the subphase prevent a straightforward replacement of EG with any aprotic solvent.[30] Table 3.1 lists some alternative subphases and their various physical properties.

From Table 3.1, we can see that sulfolane, $(CH_2)_4SO_2$, is the closest to EG in both surface tension and viscosity values; and because the only H atoms in this molecule are part of completely nonpolar C-H alkane bonds and thus cannot be donated protons, this solvent is considered aprotic. Furthermore, the listed solvents dimethylsulfoxide (DMSO), propylene carbonate, and

acetonitrile, result in poor spreading of the QD solution upon deposition, most likely because they differ too much from EG in terms of surface tension and viscosity, among other physical and chemical factors, despite the similar density values and nonreactivity to the QD film.

Subphase	Surface tension (mN/m)	Viscosity (mPa s)
EG	48.4	16.1
sulfolane	47.7	6.3
n-methyl-2-pyrrolidone	42.6	1.89
dimethylsulfoxide	42.9	1.99
propylene carbonate	40.9	2.50
acetonitrile	28.7	0.37

Table 3.1*: List of explored alternative subphases for QD self-assembly.*

Some evidence in support of this was found in the addition of small amounts (5 – 10 wt%) of polymethylmethacrylate (PMMA) to DMSO, which successfully increased the viscosity of the subphase and led to better QD solution spreading. However, upon injection of the EDA solution, the PMMA in the DMSO subphases becomes insoluble and precipitates out of the subphase. While this issue can be overcome by changing the EDA solvent, sulfolane is a simpler choice, with only a singular component and an optional heating step as the only extra preparation procedure before use. Furthermore, it facilitates a decent enough spreading of solution on its own and is able to produce an appropriate area of film with a uniform thickness that can be tuned accordingly via the QD solution concentration. Examples of the discussed reasonable alternative subphases to use based on visual evaluation of uniform QD solution spreading are shown in the photos of Table 3.2.

DMSO	DMSO (5 wt% PMMA)	DMSO (10 wt% PMMA)	sulfolane
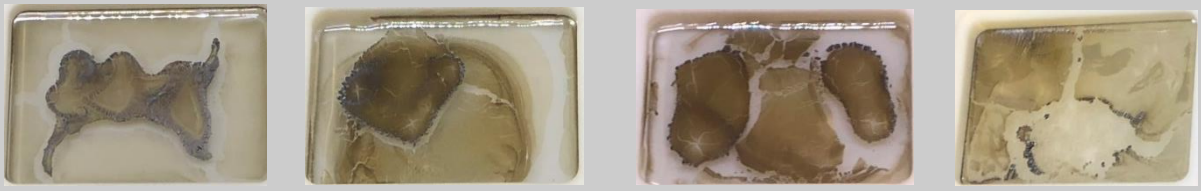			

Table 3.2: *Photos of oleate-capped SLs deposited on various subphase compositions. The concentration of the QD solution is constant for all four scenarios, but different spreading patterns, areas of uniform thickness, and average film thickness are observed.*

Because sulfolane's melting point is slightly higher than room temperature (27.5 °C), the sulfolane subphase is kept in the liquid state throughout the process by adding a 1% volume of DMSO. Additionally, because the usual injection of EDA in acetonitrile solution results in uneven epi-SL formation – perhaps due to acetonitrile's limited solubility in sulfolane, the EDA solvent was also switched to DMSO. The injection treatment can then proceed as usual, although much longer treatment periods (> 2 hours) are required to achieve even 50% oleate removal. The reasons for this are still undetermined, but most likely stem from the fact that glycoxide-oleate exchange is no longer taking place; ICP-MS experiments can further confirm that the main mechanism for oleate removal is now the L-type EDA chelation of the Pb-oleate complex from the QD surface, as discussed previously in Chapter 1.3.

With the development of the photobase process outlined in Chapter 2.4, exploring alternative subphases has become even more relevant. Because the currently utilized PBG molecule has a limited solubility in EG, a subphase with higher solubility is preferred so that the

PBG concentration, and thus oleate removal, can be tuned across the entire possible range (i.e., 0 – 100% removal). Current experimental efforts are directed towards n-methyl-t-pyrrolidone (NMP), which can dissolve >300 mM of the PBG molecule. In addition, its density and viscosity are similar to those of EG (as seen in Table 3.2), although preliminary explorations have revealed that the spreading dynamics of QD hexane solution on pure NMP are not an exact match. Still, ideally some mixture of EG and NMP will be able to provide a reasonable spreading and self-assembly of the oleate-capped SL, as well as facilitate a wider range of oleate removal and shorter exchange times overall via the glycoxide-oleate exchange mechanism.

3.2 CHOICE OF QUANTUM DOT SOLVENT

In the self-assembly process, the QD solvent is just as important as the subphase solvent. The choice is narrowed down to relatively nonpolar solvents – meaning solvents with a small or zero dipole moment – as the oleate ligands capping the surface of each QD after synthesis are long, nonpolar hydrocarbon chains. This means that alkane solvents, such as hexane and octane, are preferred over more polar solvents, such as toluene, as they are better able to solvate the QDs and thus prepare films of higher structural quality. The effects of solvent polarity can be seen in Figure 3.2, where an oleate-capped SL self-assembled on EG from hexane and toluene solutions, respectively, are compared. The QDs dissolved in hexane assembled into a film of more uniform thickness, while the QDs assembled from the toluene solution aggregated more aggressively, creating an islanding effect in the bulk film, and thus large thickness gradients across micron length scales.

Vapor pressure of the QD solvent is also important. As discussed in the previous section, the EG subphase begins to remove oleate from a floating film after >10 hours of exposure time.

Therefore, a solvent with an extremely low vapor pressure can still hinder the self-assembly of a uniformly thick film even if is extremely nonpolar. For example, an oleate-capped SL assembled from an octane solution takes more than triple the amount of time to dry than a film assembled from hexane. As a result, the octane film also displays some thickness gradients akin to the toluene film (see Figure 3.2). Unlike toluene, which produced islanding with the same drying time as that of hexane because its higher polarity most likely decreased the QD's solubility and encouraged the QDs to precipitate from solution in aggregates instead of a controlled self-assembly of uniform thickness throughout, octane films possess islanding as an exclusive function of drying time, possibly due to contraction of the film as the EG begins to remove oleate from the film during the hours it takes to assemble and for the octane to evaporate.

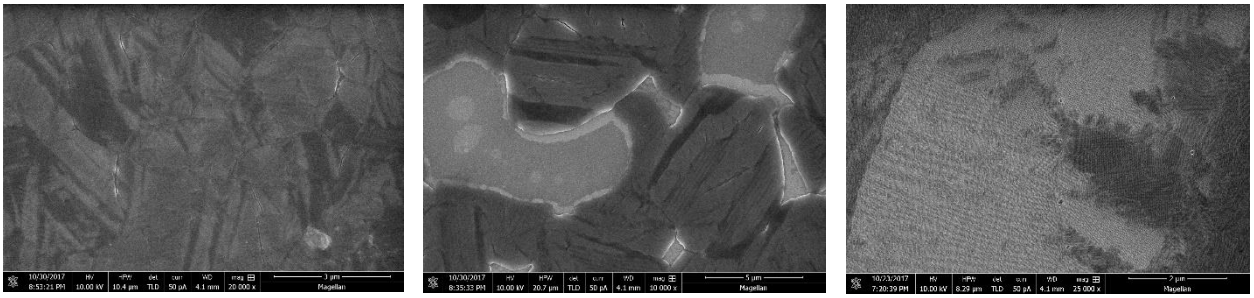

Figure 3.2: *Plan view SEM images of oleate-capped films deposited from (left) hexane, (middle) toluene, and (right) octane solutions of the same QD concentration. Changes in contrast within the image indicate a change in thickness of the QD film. The light gray areas in the toluene image are the bare substrate, meaning that the film is exhibiting extreme islanding effects.*

It should be noted that there are some applications for which more polar solvents, or higher boiling point solvents, are preferred over hexane, such as the (electro)spray deposition of QD films that will be touched on in the discussion of future work in QD SL fabrication in Chapter 5. However, for the purposes of drop-casted self-assembly of QD SLs, a low boiling point, extremely nonpolar solvent such as hexane is the best choice for making QD solutions.

3.3 FILM THICKNESS

While most self-assembled QD SL studies have been confined to mono- or bilayers,[7,12,24] this dissertation has shown that controlled self-assembly of multi-layer films is readily achievable. In fact, by tuning the QD solution concentration and deposition volume, films over 1 micron in thickness can be fabricated using the same self-assembly procedure, which is a promising prospect considering the practical need for thicker films in any electronic device implementation of the epi-SL.

The relationship between QD concentration and the resulting film thickness is dependent on the material and size of the well containing the subphase. The polarity of the well material will affect the contact angle the EG subphase has with the well walls, resulting in either a convex or concave surface curvature. Teflon, for example, is nonpolar, resulting in a high contact angle with the polar EG subphase and a convex surface that allows the QD solution deposited in the middle of the surface to spread easily to the sides. This spreading dynamic manifests because of the slight downward slope of the surface, as well as the matching polarities that attracts the nonpolar QD solvent to the Teflon sides of the well. Conversely, if the well is made of quartz – such as the petri dish used for the photobase fabrication method described in Chapters 2 and 6 – then this more polar material creates a smaller contact angle with the EG at the well walls and forms a concave subphase surface instead. In this case, the QD solution must be deposited evenly around the circumference of the well in order to ensure a smooth and uniform solution spreading; the QD solution is very easily drawn to the center of the EG surface now due to the concavity and because the QD solution is attracted more to other QD solvent molecules than to the polar quartz material. If the QD solution is deposited in the center of the petri dish, it would dry as an aggregate instead

of spreading thinly, leading to a dense, uneven, low-spatial order film upon drying. Thus, QD solution concentrations for a certain film thickness are subject to change based make of the well.

Another factor to be considered is the surface area of the well opening. A smaller surface area requires a smaller volume of QD solution. It then follows that thicker films should be achievable by depositing larger QD solution volumes and/or QD solutions of higher concentrations; however, this is not strictly true in practice. The amount of QDs needed to make a solution of high enough concentration to achieve micron film thicknesses is sometimes not reasonable in terms of practical material usage; it is more cost-effective and efficient to use higher volumes of less concentrated solution. In experiment, thicker films can be fabricated by depositing successive amounts of a smaller volume of QD solution, waiting for each addition of new solution to dry before depositing the next round. While the subsequent depositions of new solution will inevitably re-dissolve at least some of the previously dried film, the finished oleate-capped SL can still maintain a uniform thickness. Flooding the well with a copious amount of QD solution, i.e., equivalent to the sum total of all the individual additions of the successive deposition method, may result in slower drying, which would affect the self-assembly due to longer exposure to EG, and lead to a much higher variation in thickness across the entire film.

Each of the above factors must be carefully considered and optimized to fabricate a film of any desired thickness. The thickest oleate-capped SL fabricated to date in this group, shown in Figure 3.3 to be almost 1.8 microns thick, was made using a single deposition of a large volume (420 µL versus the 60-90 µL used for a 40-80 nm thick film) of medium concentration of QD solution (30 mg/mL versus the usual 10-30 mg/mL, but concentrations of 100 mg/mL can also be easily achieved in hexane) self-assembled in a Pyrex petri dish. The thickest epi-SL, also shown

in Figure 3.3, was made using 180 µL of 30 mg/mL in the usual Teflon well and then exchanged for 60 seconds after EDA injection.

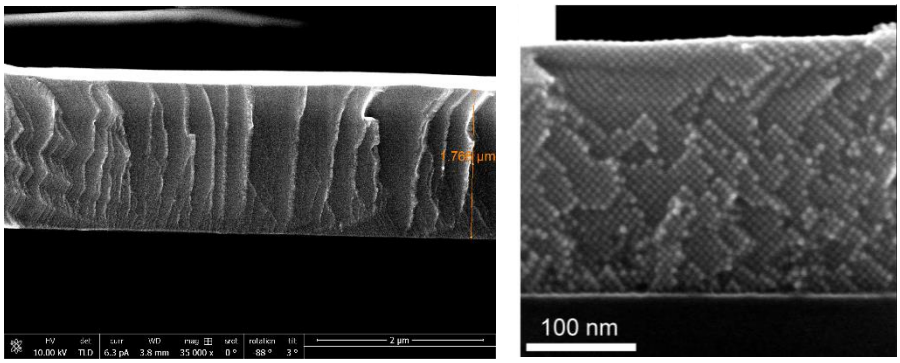

Figure 3.3: *(left) Cross-section SEM image of a 1.8 µm thick oleate-capped SL. (right) a higher magnification cross-section SEM image of a 230 nm thick epi-SL.*

Due to a variety of possible factors, such as the increased mass of the film or the increased surface roughness that is observed with thicker films start at ~200 nm thickness, simple Langmuir-Schaefer stamp transfer of the film to a silicon substrate results in significant delamination, i.e., the film failing to completely transfer to the solid substrate surface. This was solved by using a polydimethylsiloxane (PDMS) stamp intermediate step, wherein the film is easily transferred to a piece of clean PDMS, and then stamped onto the desired silicon substrate by applying sufficient and even force to the back of the PDMS before peeling it off. Any additional effects of this intermediate step are unknown; there may be organic debris left over from the PDMS transfer, and the observed roughness of the film surface in plan view SEM cannot be distinctly attributed to the PDMS transfer step nor the self-assembly process.

Fabricating films on the micron scale of thickness is essential for epi-SLs to be practical for optoelectronic devices and photovoltaics. Due to the nature of the self-assembled epi-fusion process, there may exist a maximum thickness that can be uniformly fused into the epi-SL, because

the chemical trigger must travel from the subphase on the liquid/film interface side of the epi-SL upwards to the film/atmosphere interface. Currently, epi-fusion has been achieved for films of ~230 nm thickness, and thicker films can be a useful tool for studying exchange gradients and dynamics inherent in the epi-fusion of self-assembled SLs, as will be further elaborated on in Chapter 5.

3.4 QUANTUM DOT OLEATE COVERAGE

The oleate coverage of QDs after synthesis and purification has been shown to have some influence on the resulting self-assembly of oleate-capped SLs. The choice of purification solvents used on QDs after synthesis has a direct effect on the resulting oleate coverage; for a conventional purification using ethanol and hexane, the ethanol strips oleate with each successive wash and leads to a more distorted simple cubic epi-SL structure.[9] Furthermore, epi-SLs that are fabricated using ethanol-washed QDs possess grains on the order of just 500 nm. Such a length scale greatly hinders charge transport measurements of the epi-SL; for a FET channel typically 25 microns in length, a charge must then overcome ~50 grain boundaries in traveling the channel, not including other scattering centers and trap states.

To overcome this issue, purification using acetonitrile and toluene has been shown to be a much gentler process, requiring 9 purification cycles instead of 2-3 but ultimately resulting in a much higher oleate coverage for the QDs. The immediate benefit of this processing change is the increase in oleate-capped SL grain size, up to a maximum observed size of ~5 microns. Slight tuning of the QD solution concentration is also required because of the change in spreading dynamic on the EG subphase surface; while the ethanol-washed QDs spread radially from their deposition point towards the Teflon well walls, the acetonitrile-washed QDs are more likely to

flow and meander in solution across the EG until they meet the Teflon and eventually spread to cover the entire subphase surface. This extra meander may also be the source of extensive twinning observed within the micron-sized grains; these are still undesirable when it comes to charge transport. Therefore, further improvements must be made to the oleate-capped SL fabrication process, i.e. defect-free grains on the scale of ~10 microns, in order to ensure near-perfection in the resulting epi-SL and thus the further study and improvement of its charge transport.

CHAPTER 4 : FURTHER STUDIES ON QUANTUM DOT EPI-FUSION

4.1 ALTERNATIVE X-TYPE LIGAND EXCHANGES

The glycoxide-oleate exchange is not the only X-type ligand exchange that can occur in QD SLs. The PbI_2 soak after the EDA injection treatment reported previously in Chapter 2.1, for example, is most likely an X-type ligand exchange with iodide, as it causes a decrease in both the oleate and glycoxide FTIR signals.[9] This could be confirmed with future ICP-MS experiments to determine the presence of extra Pb^{2+} in the PbI_2 / DMSO solution after soaking the epi-SL.

Iodide is not the only halide that can undergo X-type ligand exchange with the surface oleate. Injection experiments with ammonium chloride, bromide, and iodide (87 mM total halide salt in the subphase) have shown that comparable oleate removal and epi-SL formation to those of EDA injection is possible, albeit over longer time scales, as seen in Figure 4.1.

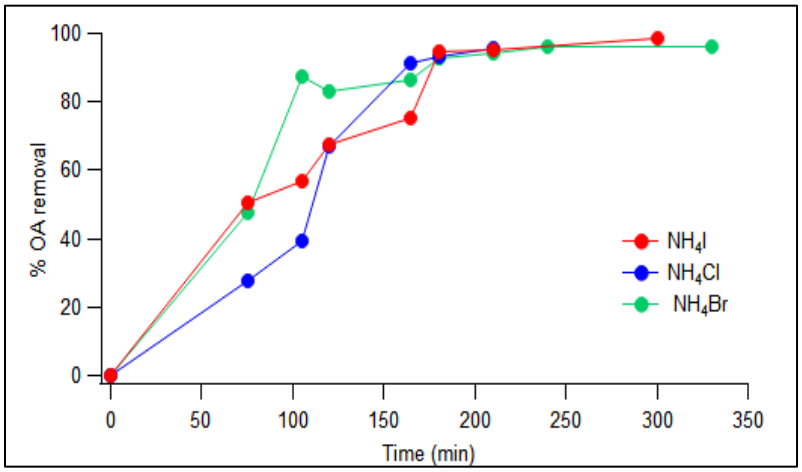

Figure 4.1: *Oleate removal as a function of time for epi-SLs made by ammonium halide injection.*

The ammonium halides are much slower to remove oleate, taking almost 180 minutes (3 hours) to achieve >90% removal. Although the glycoxide-oleate exchange is also X-type, the oleate removal kinetics are much faster despite the lower concentrations of chemical trigger (e.g., ~9 times faster for ~2 times the amount of trigger injected into the subphase). There are several possible reasons for this difference. First, the chemical equilibrium of the X-type exchange taking place defines the extent of favoring of the reaction's products, i.e., the oleate salt that is formed upon oleate's removal from the surface, as well as how likely the replacement anion will bind to the QD surface. Thus, the ammonium oleate, i.e., the corresponding salt after the halide anion exchanges with the oleate on the QD surface, could be less favored to form than either the amine oleate (in the case of the amine-triggered glycoxide-oleate exchanges) or water (in the case of hydroxide-triggered glycoxide-oleate exchanges). It could also be that the halide ion itself has a lower affinity for the QD surface than glycoxide does.

Another factor that could affect the exchange kinetics is the diffusion of the ammonium halide compound into and out of the SL. Because ammonium is a much smaller cation than the cations produced by the glycoxide formation, it's possible that ammonium is of an appropriate size to compete with the iodide in diffusing through the pores of the epi-SL, causing a slower overall exchange with the surface oleate. Some FTIR spectra collected from these epi-SLs have indeed shown peaks in the amine N-H region, indicating residual ammonium ion in the film that sometimes remains permanently in the ammonium-halide-treated epi-SL.

Besides the ammonium halides, successful X-type ligand exchange has been performed using anions such as thiocyanate (SCN^-) and formate ($CHOO^-$), especially in short-range order or amorphous QD films. Unfortunately, narrow ranges of workable concentrations within the current self-assembly system have limited their current use in epi-SL formation. Ethanethiol (CH_2CH_2SH)

is also an option and has produced similar results to that of EDA and its glycoxide-oleate exchange. Although currently limited to utilization via the injection method, it has further promise as a secondary treatment if it is able to replace glycoxide on the surface such that H_2S treatment and subsequent ALD alumina infilling may produce a completely inorganic epi-SL.

4.2 GRAIN MAPPING OF OLEATE-CAPPED AND EPI-SLS

Categorization of grain sizes and intra-grain defects is essential to the study of epi-SL charge transport. In order to gather meaningful statistics of the types of grain boundaries, sizes, and defects observed, mapping of large SL areas (ideally ~100 microns in length, a scale that should increase as fabrication methods improve and subsequent grain sizes increase) is an important and ongoing effort.

Preliminary grain maps of both oleate-capped and epi-SLs, shown in Figure 4.2, display a noticeable contrast in defect distribution and density before and after oleate removal. The oleate-capped film shows grains with edges on the order of 5 microns, some with defects (e.g., partial twins, meanders/random structural jitter) and others with large pristine areas, emphasized by the visible unbroken interference patterns (Moiré patterns caused by the stacked layers of QDs just slightly offset from another because of their unit cell structure) shown in the SEM images. The epi-SL grain map, however, implies that the structural transformation as a result of ligand removal causes the formation of even more structural defects and results in a smaller average grain size than that of its parent SL.

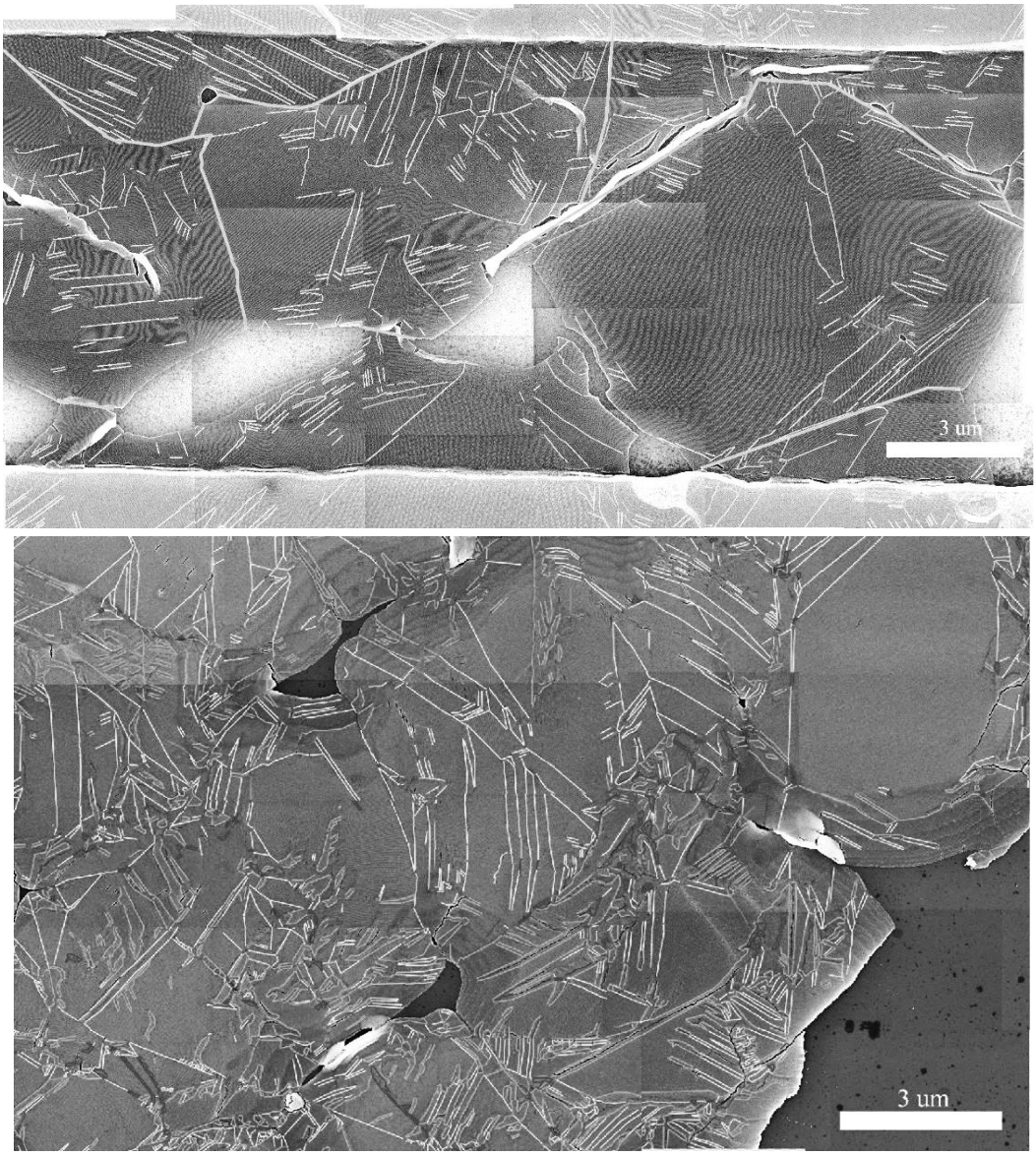

Figure 4.2: *Grain maps of (top) an oleate-capped SL and (bottom) an epi-SL. White lines on the grayscale film indicate grain boundaries. The darkest gray areas in each image are the substrate; the two lighter rectangles running along the top and bottom edges of the oleate-capped map are gold electrodes underneath the film.*

Further image and structural analysis of the epi-SL grain maps provide specific insight into the types of grain boundaries that can form, and at what frequencies. As mentioned in previous chapters, the epi-SL self-assembles such that the (100) or (01-1) SL planes are parallel to the surface, and thus visible in plan view SEM. For the following statistical analyses, the (01-1) SL

orientation is more pervasive throughout the studied films; in general, the factors that influence SL orientation remain unclear, but may have to do with such factors as the starting oleate coverage of the QDs, or the thickness of the film; a direct correlation between oleate coverage and the occurrence of (01-1) SL grains has been tentatively observed.

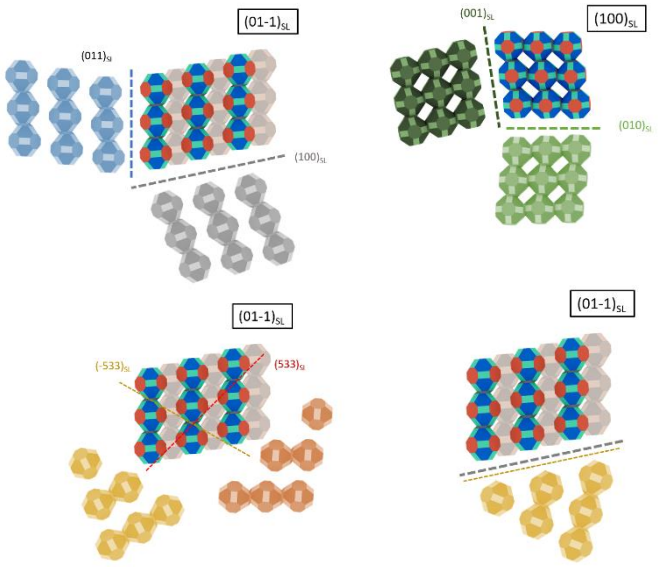

Figure 4.3*: Primary bisecting planes of the (100) and (01-1) epi-SL orientations observed in the formation of grain boundaries. (top, left) Grain boundaries formed by the bounding planes of (left) the (01-1) and (top, right) the (100) epi-SL grains. (bottom, left) The {533} family of bisecting planes of the (01-1) orientation, and (bottom, right) an example of such a grain boundary formed by this family.*

Because neighboring QDs are expected to fuse along their {100} facets, the resulting boundaries between adjacent grains will be primarily limited to the junctions of a few select planes that bisect the (01-1) SL orientation. As seen in Figure 4.3, a boundary between two (01-1) grains can be formed by the meeting of either grain bisected by a plane of the {011} or {533} families, leading to seven possible observed grain boundaries for this epi-SL orientation. Further manual examination of the unit cell model shows that each of these grain boundaries are likely to fuse

across either a QD's {100} or {110} facets, according to Table 4.1. It should be noted that while a grain boundary across the (011) plane does occur, other grain boundaries are unlikely to form alongside this bisection, possibly due to the significant misalignment of the QDs' facets most parallel to that plane. In addition, the twin defined by the (533) plane fuses across only the {110} facets, and thus can be expected to rarely occur due to the higher surface energy, and thus more difficult oleate removal, of these facets in comparison to the {100}.[5] The (100) epi-SL orientation, meanwhile, has two observed grain boundaries, either across the (001) or the (010) planes.

Grain boundary	**QD facet(s) being fused**
$(100)_{SL}$ twinning plane	{100}/{100}
$(-533)_{SL}$ / $(100)_{SL}$	{100}/{100}
$(011)_{SL}$ twinning plane	{100}/{110}
$(-533)_{SL}$ twinning plane	{100}/{110}
$(533)_{SL}$ / $(100)_{SL}$	{100}/{110}
$(533)_{SL}$ / $(-533)_{SL:}$	{100}/{110}
$(533)_{SL}$ twinning plane	{110}/{110}
$(001)_{SL}$	{100}/{100}
$(010)_{SL}$	{100}/{100}

Table 4.1: *Grain boundary type and their corresponding fusing facets. The bottom two rows are boundaries observed in the* $(100)_{SL}$ *orientations.*

Examples of all observed grain boundaries are shown in Figure 4.4, each SEM image overlaid with scaled models of the depicted QDs and the boundary in between. With the types of observable grain boundaries now defined, manual image analysis of SEM grain maps taken of

sample films can be carried out to compile statistics on the occurrence of each grain boundary type. Grain boundary distributions of one EDA injection epi-SL and two epi-SLs fabricated via photobase trigger are shown in Figure 4.5. From these plots, a few observations can be made. First, the general distribution indicates the most common grain boundary to be across the (100) plane, which makes intuitive sense because this boundary exhibits direct fusion across {100} facets; thus, most of the total grain boundary length of each sample is also made up of these boundaries.

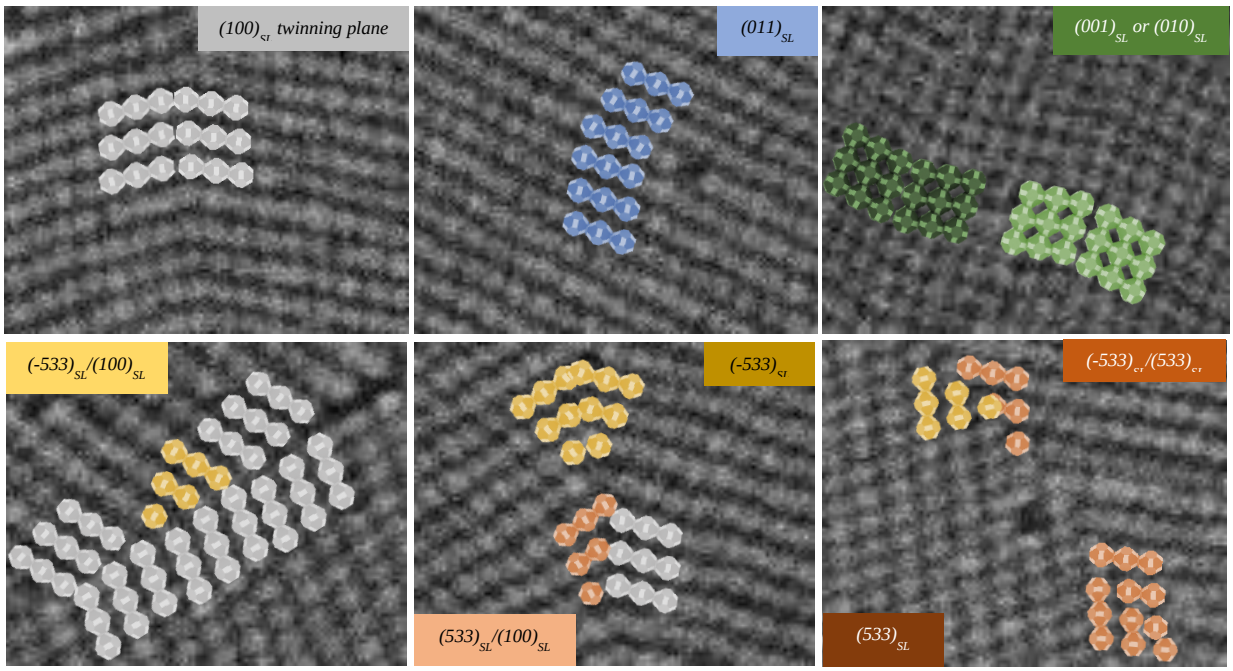

Figure 4.4: *Observed epi-SL grain boundaries. Labeled according to the bisecting plane on either side of the depicted grain boundary. All epi-SL orientations depicted are (01-1) except for the top right, which is (100)SL.*

Of similar population, however, are the grain boundaries across the (011) plane. These often manifest as partial twins within a particular grain, meaning that the boundary is incomplete and corrects itself to the orientation of the surrounding grain area before it meets a boundary such that a separate grain is formed; it should be noted that these are the primary occurrence of a "partial" grain boundary, and other observed grain boundaries tend to enclose complete grains.

The ratio of (100) to (011) boundaries for a particular epi-SL is not yet defined, requiring a much higher sample size and possible differentiation between epi-SL fabrication method. The other grain boundaries observed in $(01\text{-}1)_{SL}$ grains are made up of combinations with boundaries defined by the {533} family of planes.

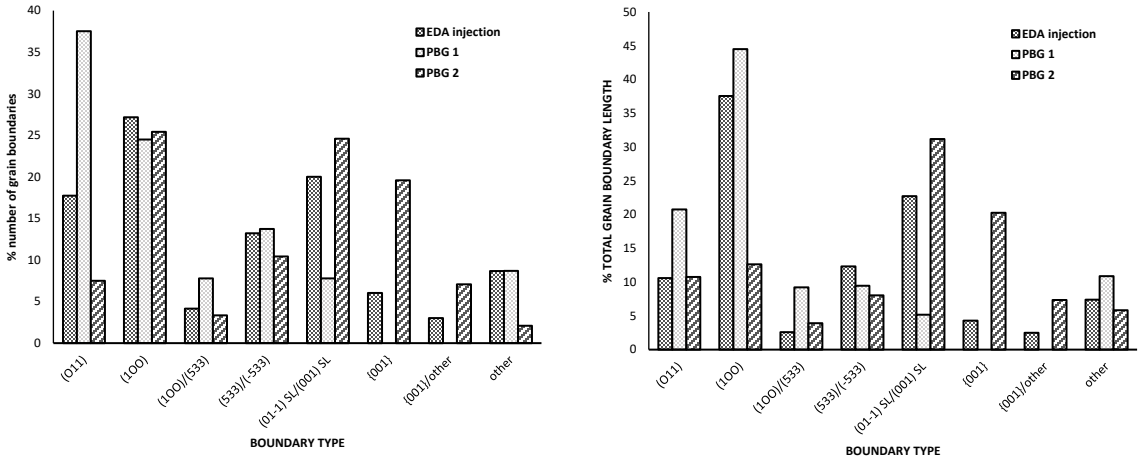

Figure 4.5: *Grain boundary distributions for three different epi-SL films. The "{001}" and "{001}/other" categories are exclusive to the* $(100)_{SL}$ *orientation; all other boundaries are for the* $(01\text{-}1)_{SL}$ *orientation.*

Because the distribution of $(01\text{-}1)_{SL}$ and $(100)_{SL}$ grain orientations differ across the sampled films, different distributions of grain boundaries associated with the $(100)_{SL}$ grains will result. Thus, while the first photobase sample ("PBG 1" in Figure 4.5) was almost entirely the $(01\text{-}1)_{SL}$ orientation, resulting in no observable $(100)_{SL}$ related grain boundaries, "PBG 2" and "EDA injection" had a 20-40% population of $(100)_{SL}$ oriented grains, which subsequently contributed similarly to the overall grain boundary distribution.

The above categorization is complicated by further structural disorder that can propagate throughout the film. For example, one observed boundary between two grains may, upon closer inspection, meander between a few different boundary types along its length. Figure 4.6 shows

how one boundary between two $(01\text{-}1)_{SL}$ grains is technically three connected boundaries of different types. These types of subtleties are difficult to express in manual analysis and must be carefully considered when drawing any proper conclusions about grain boundary distributions of any SL film.

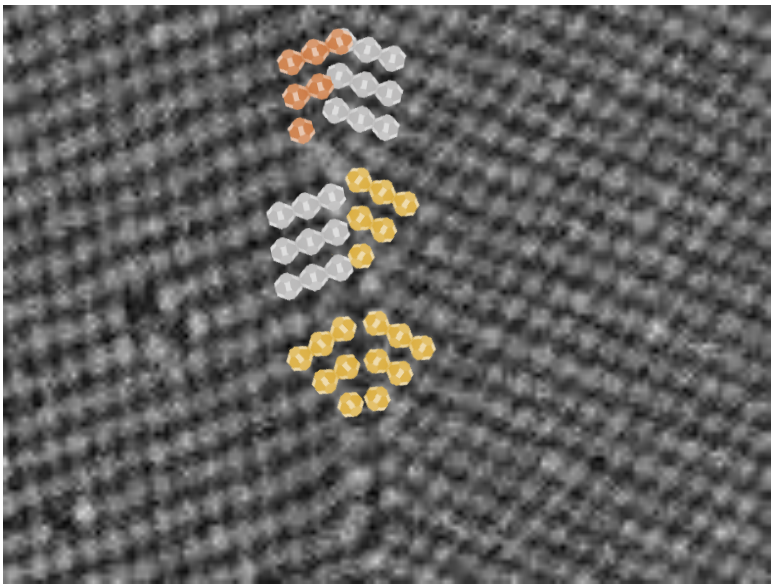

Figure 4.6: *Grain boundary between two $(01\text{-}1)_{SL}$ grains exhibiting three boundary types. From the top of the image, the boundary meanders from (533)/(011) to (011)/(-533) to (-533) twin; this results from several point defects observable along the boundary.*

This preliminary attempt at grain mapping and subsequent classification of the observed boundaries and structural defects reveals the importance of understanding defect formation so that it can be mitigated to create monocrystalline epi-SLs. Analysis of the same epi-SL films presented previously shows a ~20° deviation from the expected grain boundary angle created by two joined chains of QDs in the (01-1) epi-SL orientation. To create such a tilt, even at a theoretically perfectly angled grain boundary, the QD {100} facets are not in fact completely co-facial, but meet at an angle as depicted in Figure 4.7. Preliminary modeling of two neighboring QD {100} facets via the

CrystalMaker software shows that 1-3 (partial) layers of QDs between the adjoining facets is enough offset the boundary angle to the desired value. This is dependent on the width of the facet, which has been determined via atomically resolved TEM to be ~2.4 nm for a QD of 6.5 nm diameter.[31] In fact, if the facet width is extended to 3.7 nm to match recent epi-SL tomography data,[32] a thickness of up to 4 extra QDs in between the fused facets will be required to achieve the same angle. While more rigorous simulations must be performed to confirm these scenarios, the investigation shows that a defect as small as one extra QD on the facet surface may have a significant impact on subsequent fusion and epi-SL monocrystallinity.

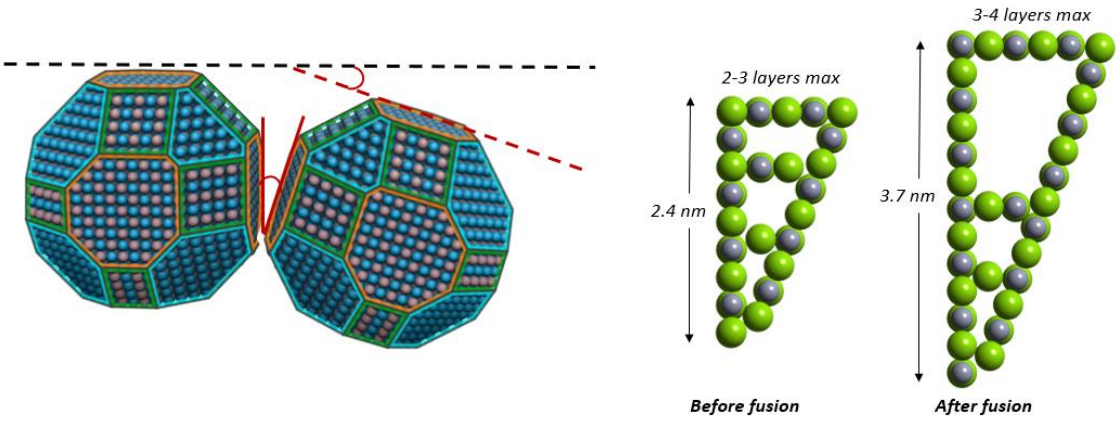

Figure 4.7: *(left) Two QDs tilted to create the SEM observed boundary angle, in red. (right) CrystalMaker depictions of the QD-size defects needed between two adjacent facets to create this boundary angle.*

4.3 EPI-SL SINGLE GRAIN FLAKE COLLOIDAL SOLUTIONS

In an effort to achieve mini-band formation in these QD epi-SLs, electronic measurements of single grains have become imperative in understanding the physics of charge transport within these materials, as well as evaluating progress and improvement in epi-SL fabrication methods.

Creating colloidal solutions of single grain epi-SL flakes to deposit on a desired substrate is one approach to achieving this.

The process is depicted in Figure 4.8. First, a bare silicon substrate is treated with a self-assembled monolayer (SAM) such as octadecyltrichlorosilane (ODTCS), a long hydrocarbon chain with three chloride groups on one end that will adhere to the Si surface. Gentle annealing of the treated substrate will remove water and encourage the formation of a well-ordered, dense SAM of ODTCS. This treated Si can then be used to stamp an epi-SL floating on the EG subphase. After excess EG and EDA solution is rinsed from the film using clean acetonitrile ("MeCN" in the figure), before it is submerged in a vial of fresh MeCN and sonicated. Because the epi-SL has been deposited onto a hydrophobic surface, upon sonication it will delaminate from the substrate more easily and shatter into flakes. While shattering along grain boundaries isn't guaranteed, the resulting flakes are indeed mostly single grain, and upon deposition onto any desired FET substrate for electronic measurements, some random distribution of flakes that are both single grain and of the desired size should be present.

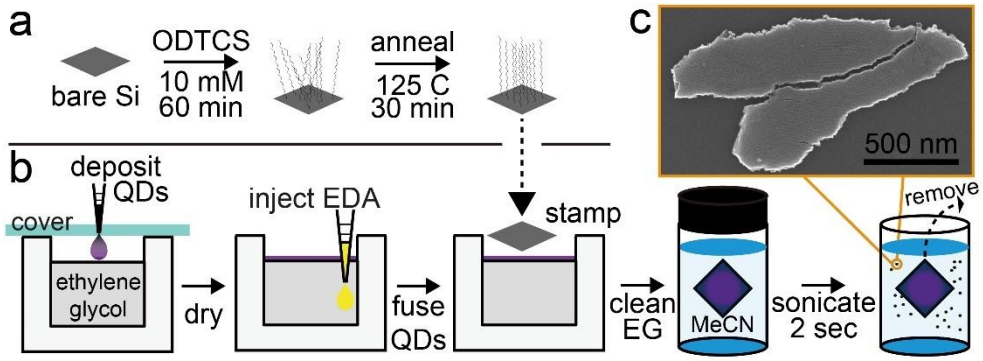

Figure 4.8: *Schematic depicting the fabrication of a colloidal epi-SL flake solution.*

There are several optimizations of this process that have yet to be fully realized. First is the substrate treatment itself; a balance must be achieved with regards to the SAM's hydrophobicity,

and thus delamination capability, such that the epi-SL will be successfully transferred to the substrate and will only peel off at the sonication step. Molecules more hydrophobic than ODTCS, such as its fluorinated semi-analog, perfluorodecyltrichlorosilane (FDTS), or the significantly shorter trifluoromethyltrimethylsilane (TMTFS), yielded better results, but the produced flakes remained on the order of ~400 nm in length and sometimes were coated in residue – possibly from the SAM.

Another method explored as an alternative to the hydrophobic self-assembled monolayer is to spin coat a sacrificial layer of PMMA onto the Si substrate. Once the epi-SL has been stamped onto the PMMA, the deposited film and substrate can be submerged in tetrahydrofuran (THF), which will then dissolve the PMMA and cause the film to be shattered in the process. Despite the PMMA remaining in the final flake solution, deposited flakes from this method were relatively

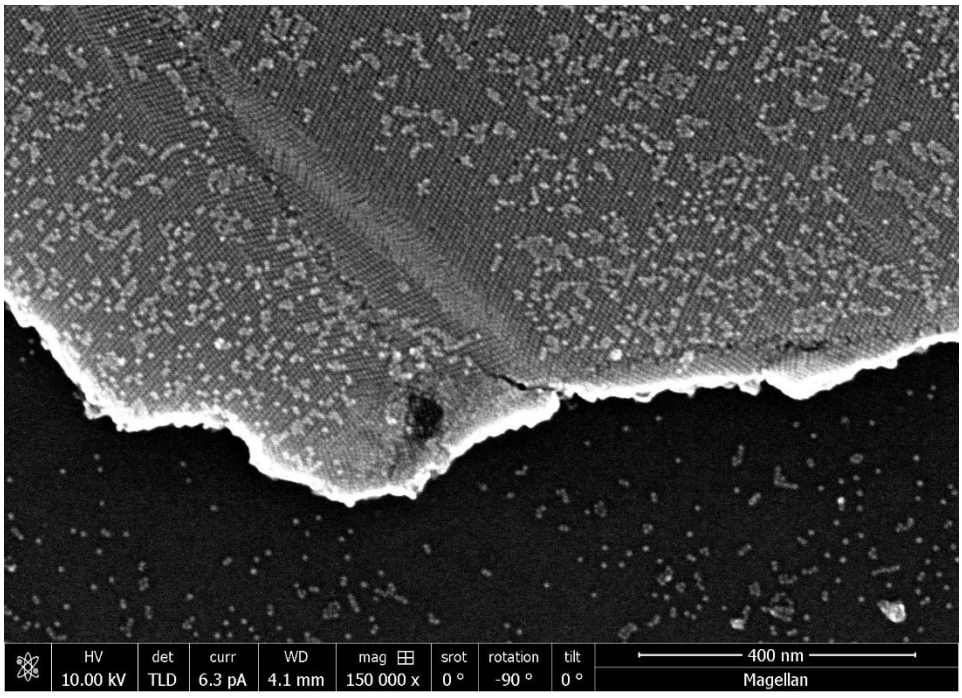

Figure 4.9: *Plan view SEM image of a deposited single grain flake from the PMMA process. The flake is extensively covered with small QD clusters and individual QDs, which will eventually fuse together and cause immense contamination upon several days of storage as a solution in THF.*

clean, with the exception of scattered individual QDs or small QD clusters additionally deposited onto and near the flakes, as seen in Figure 4.9. However, aging of this solution yielded strong contamination and possible fusion of the QDs within and adjacent to the flakes, and so was ultimately determined to not be a viable method.

Apart from this effort, another procedure to electronically measure single epi-SL grains has been developed by the group and has seen reasonable success (manuscript in preparation as of May 2022), effectively shelving the immediate need for continued research into epi-SL flake solutions. Still, development of this method may be considered further in the future, as a successful method for producing colloidal flake solutions would pave the way for fast and reliable measurements of dozens of single grain devices within a single drop.

CHAPTER 5 : FUTURE WORK

5.1 PERFECTING THE EPI-SL

Portions reprinted with permission from ACS Nano 2022, 16, 2, 3239-3250. Copyright 2022 American Chemical Society.

Overall, the main body of this dissertation shows that conversion of oleate-capped PbSe quantum dot superlattices into epitaxially fused superlattices by the standard method of amine treatment in the presence of an ethylene glycol subphase is mediated by glycoxide–oleate ligand exchange. In this mechanism, the amine deprotonates ethylene glycol to form glycoxide, which then replaces oleate on the QD surface, decreasing the inter-QD spacing and triggering fusion across the {100} facets to form the epi-SL. The percent oleate removal, inter-QD distance, and degree of epi-fusion are strongly correlated with amine pK_b in ethylene glycol, suggesting that the glycoxide concentration (dose) drives epi-SL formation. Essentially identical results were obtained by replacing the amines with tetrabutylammonium hydroxide. Quantitative agreement between the amine- and hydroxide-treated films in terms of oleate removed, inter-QD spacing, and Ψ_4 as a function of [glycoxide] establishes that the glycoxide dose is the single most important factor governing epi-SL conversion, and the epi-SL phase transition occurs abruptly at a threshold glycoxide concentration (~200 μM at these conditions).

The insight that epi-SL conversion is mediated by a Brønsted–Lowry acid–base reaction between the injected base (amine or hydroxide) and ethylene glycol was then leveraged to propose photobase triggering as a fundamentally better way to make epi-SLs. FTIR and SEM mapping showed that bottom UV illumination of a piperidine-producing photobase generator dissolved in

the ethylene glycol subphase resulted in epi-SLs with excellent chemical and structural uniformity compared to the highly inhomogeneous epi-SLs made by piperidine point injection, the latter of which exhibited strong lateral gradients in oleate coverage, inter-QD distance, and epi-fusion. Photochemically made films not only are more uniform but also contain much lower concentrations of small extended structural defects such as tears and cracks, probably in part because photobase illumination is contactless and avoids the damaging mechanical disturbances caused by point injection. Statistical analysis of SEM images showed that photobase-made films have five times fewer nanotears, 17 times fewer chain splits, and six times fewer intraflake cracks compared to injection-made films with equivalent values of oleate content, inter-QD distance, and Ψ_4. The structural–chemical uniformity and structural perfection of these photobase-made epi-SL films make them leading candidates for achieving emergent mini-band charge transport in a self-assembled mesoscale solid. Thus, the reported photochemical-triggering approach also provides a way to scale up epi-SL fabrication and implement (low-resolution) photopatterning for optoelectronic devices.

Previous work has suggested that amines remove Pb from PbX QDs floating on EG,[12] but the evidence for Pb removal (subtle changes in UV–vis spectra, TEM size histograms, and energy dispersive spectra after treatment with *n*-butylamine) was indirect and inconclusive. Direct measurements of Pb removal (*e.g.*, by ICP-MS) should be performed to determine the relative importance of the Lewis and Brønsted mechanisms for a greater number of amines. Based on the work presented in this dissertation, *n*-butylamine (pK_b = 3.4 in water and probably ∼4.0 in EG, similar to EDA and piperidine) is expected to act similarly to EDA and removes oleate by glycoxide–oleate exchange rather than complexation with lead oleate.

There are several possible explanations for the lower concentration of chain splits, nanotears, and intraflake cracks in the photobase-made films. First, since photochemical triggering avoids the mechanical disturbances caused by point injection (e.g. vibrations and bulk liquid flow), the photobase-made films may suffer less mechanical damage. Second, differences in ligand exchange dynamics may result in fewer defects in the photobase-made films. In particular, it is likely that the laterally uniform and slower ligand exchange enabled by photobase illumination produces less mechanical stress in the film compared to the radial concentration gradient and propagating reaction fronts inherent to point injection. A third possibility is that the photobase-made epi-SLs are mechanically stronger and therefore less damaged when stamped from the EG surface to a solid substrate. While it is clear that photobase-made films have far fewer extended defects than do the injection-made films, it cannot be determined from the current data exactly why this is the case. Further experiments comparing the two fabrication methods in terms of defect densities and distributions across various levels of oleate removal will need to be conducted in order to definitively identify the cause(s) of this observed difference.

5.2 PERFECTING THE OLEATE-CAPPED SL

While photochemical triggering may offer a convenient way to spatiotemporally tune the glycoxide dose and control the exchange kinetics to reduce the concentration of cracks and tears arising from volume loss, it is ultimately the structural perfection of the parent oleate-capped SL that determines the concentration of extended defects in the epi-SLs. Cracks tend to form at weak spots in these films, such as along SL grain boundaries. Therefore, the most promising way to make less defective epi-SLs is to increase the grain size and improve the intragrain spatial order of the oleate-capped SLs, which is the focus of future work on this project. Specific plans include

implementing a(n) (electro)spray deposition system, by which a solution of QDs will be gently sprayed upon the EG surface. The aerosolization of the QD solution, which can also be achieved via application of an electric field, will lead to nanometer-sized droplets that will minimally disturb both the subphase surface as well as the surrounding solution droplets. In this way, an extremely uniform film can be deposited over much larger areas than what is currently being achieved with manually deposited self-assembly. Spray deposition has already been achieved with QDs in long-chain alkanes, albeit in air and deposited on micron-sized droplets (~30 μm in diameter) of subphase, or on a solid substrate and resulting in short-range order.[33,34] Meanwhile, electrospray deposition of self-assembled films has been achieved for gold nanoparticles suspended in water-miscible solvents; the polarity of such solvents allows them to be ionized into smaller droplets than those achieved by conventional spray deposition.[35] However, because the QD solvent needs to be relatively nonpolar and thus may be completely or near-completely nonionizable, careful exploration of high voltage biases for the electrospray setup must be executed to determine whether only the conventional spray deposition method will be the plausible way forward.

5.3 PERFECTING MICRON-THICK FILMS

As discussed in Chapter 3.3, progression to thicker films, ideally above a micron in thickness, is ideal for real-world applications of the QD epi-SL in optoelectronic devices and photovoltaics. Thus, further parameter optimization not only of oleate-capped SL self-assembly, but also ligand exchange and stamp transfer of the epi-SL onto the desired substrate, must be pursued. Of particular importance is the limit of ligand exchange via diffusion upwards through the film from the subphase. At this time, whether the film sinks further into the subphase as oleate removal progresses, or whether the chemical trigger – solvated in EG – moves through the pores

of the QD film via capillary-like action, is still undetermined. However, thicker films could provide further insight into this aspect of the ligand exchange mechanism occurring in this system. So far, preliminary vibrometry experiments to ascertain whether a height change occurs during ligand exchange (versus no change if the capillary mechanism is indeed the operative process) have yielded limited results, as the measurement is easily skewed by the unavoidable surface disturbance/flow and reflectivity of the EG subphase. However, the concept of such in situ experiments should continue to be pursued; in situ synchrotron GISAXS experiments have been able to monitor the change in structure from oleate-capped to epi-SL, for example, and could possibly provide similar insight if a cross-sectional experiment could be successfully designed and implemented.[36]

To explore the exchange gradient itself, cross-sectional TEM and energy dispersive spectroscopy (EDS) may prove fruitful in determining the chemical transformations as the shift to the epi-SL structure takes place and oleate is removed. Admittedly, the detection of oleate, and especially its replacement by glycoxide, may prove too difficult due to the low masses of all the elements involved (i.e., carbon, hydrogen, and oxygen), but with high-resolution TEMs and adequate expertise, the experiment is feasible, if difficult.

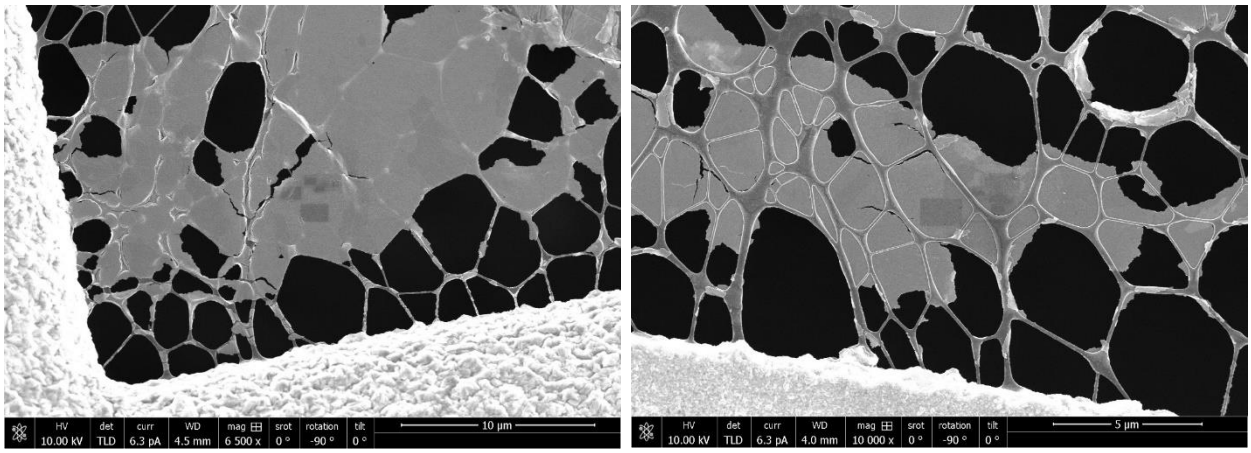

Figure 5.1: *SEM images of the (left) gas and (right) liquid interface layers of an epi-SL deposited on a TEM grid.*

Should such an endeavor prove impossible, less technically challenging methods can still offer valuable insight concerning the exchange gradient. Depositing the epi-SL on a TEM grid, for example, allows plan view SEM imaging of both the top and bottom layers of the epi-SL, as shown in Figure 5.1. FFT analyses of these images can then provide inter-QD distances of each interface layer, and thus an evaluation of the oleate removal in accordance to the methods outlined in Chapter 6.4. While this process would ignore the intermediate layers of the film (which can only be structurally analyzed via electron tomography), it should inform reasonable conclusions of the extent of the capabilities of the epi-SL fabrication process in question and how its limits can be tested and expanded in terms of final epi-SL thickness.

CHAPTER 6 : METHODS

6.1 QUANTUM DOT SYNTHESIS

Preparation of lead (II) oleate:

1. Soak the following items in the base bath overnight:
    a. Three-neck flask (100 mL) with appropriate stopper
    b. Stir bar (larger is better, but it must be able to rotate freely in the flask)
    c. Two centrifuge tubes
2. After rinsing the base bath residue off with DI water in the sink, dry everything in the oven and then set aside to cool. Ideally everything should be ~ room temperature when starting preparation for the synthesis.
3. Into the three-neck flask, measure:
    a. 1.5000 g of lead (II) oxide (PbO); this is a powder, so measure it on a weighing boat or weighing paper.
    b. 5.0000 g of oleic acid (OA); this is a liquid, so pour some out from the original container into a secondary container (e.g. a vial or small beaker) and use a 10 (12) mL syringe with purple needle (16G) to tare, and then withdraw the proper amount (~6 mL). Before taring the syringe, draw up a small amount of OA (past filling the needle) and then unload it back into the secondary container; this accounts for the dead volume, i.e., the OA that will remain in the needle even after you've emptied the syringe all the way.

c. 10.0000 g of 1-octadecene (ODE); this is a liquid, so tare a 20 (24) mL syringe with purple needle in the same way as described for OA before withdrawing the proper amount (~13 mL).

Some error is fine, but try to stay within +/- 0.0005 g of each.

4. Add the PbO, OA, and ODE into the flask along with the stir bar.
5. Add a thin line of vacuum grease along the frosted glass portion of the stopper (avoid the holes; when aligned with the spout, the flask is open) before inserting the stopper into its position at the spout of the flask. Rotate the stopper fully to make sure the vacuum grease is spread evenly along all surfaces for a proper seal.
6. Add a Keck clip to the thin end of the stopper (not the handle); this is so that the stopper doesn't slip out at any point of the synthesis. Turn the handle so that it's perpendicular to the spout (i.e. closed).
7. Seal each of the two necks of the flask with a properly sized septum. Wrap a ring of thick copper wire over the overturned septum rubber to seal it more tightly (make sure the wire doesn't slip off of the septum and onto the glass at any point); twist the ends of the wire tightly together with pliers to secure.
8. Take the flask to the Schlenk line in the fume hood. Attach the Ar/vacuum line from the Schlenk line to the spout of the three-neck flask and tighten it with the hose clamp using a screwdriver.
    a. The Schlenk line comprises of two rows – the row for Ar flow (top) and the row for the vacuum (bottom). The rows are physically separate from each other, but can both be opened to the attached flask via the appropriate valves.

9. Set the flask in a heating mantle, which should be plugged into the appropriate J-KEM power outlet, on top of a stir plate.
10. Use a clean purple needle to puncture the septum of the side neck of the flask (not the center one). Clean the thermocouple plugged into the J-KEM with hexanes/IPA and then insert it into the punctured septum; you will have to force it a little, or repuncture the septum if it won't go in, but ideally the septum should be broken as little as possible to ensure a continued tight seal. The thermocouple should be sitting in the solution as much as possible, but not resting against the flask.
11. Turn the stir plate on (somewhere 300 – 900 rpm is good depending on the stir bar size). Make sure the stir bar doesn't hit the thermocouple.
12. Make sure all the valves on the Schlenk line are closed.
13. If the cold trap to the right of the Schlenk line is not connected, check that the O-ring is present and seal the trap to the Schlenk line attachment with the U clamp (tighten all three points evenly). Ensure also that it sits in the small cylinder/dewar for liquid nitrogen (blue webbing around the outside).
14. Turn on the pump below the fume hood (red switch). Monitor the pressure gauge above the Schlenk line to ensure that the entire setup is pumping down.
15. Fill the cold trap dewar with liquid nitrogen. This will allow the base pressure to lower to ~20 mTorr eventually.
16. Open first the Ar tank valve and then, slowly, the regulator valve to the Schlenk line. Watch the oil in the gas bubbler above the cold trap to make sure the oil doesn't splash too high.

17. When the pressure is < 50 mTorr, open the vacuum valve on the Schlenk line that leads to the flask. Because the flask stopper is closed, only the hose volume is being pumped on by the vacuum.
18. When the pressure is < 50 mTorr again, slowly open the flask stopper (i.e., turn it so that the handle is parallel to the spout). The solution in the flask will start to bubble due to the sudden decrease in pressure, so wait until the bubbling settles before opening the stopper further.
19. Wait for the pressure to drop back under < 50 mTorr.
20. Once the pressure is below < 50 mTorr (this might take a while for the first pump), close the vacuum valve on the Schlenk line and slowly open the Ar valve on the Schlenk line, again watching the oil in the gas bubbler so it doesn't splash.
21. Purge the flask with Ar for ~ 60 seconds before closing the Schlenk line Ar valve once more. Carefully open the Schlenk line vacuum valve again.
22. Repeat steps 19 -21 five more times, ending with the vacuum valve open.
23. Set the J-KEM temperature (depress the * button and the appropriate arrow button simultaneously) to 120 C.
24. Adjust the power level knob as needed – the levels are labeled by solution volumes, but these are not absolute, so if the solution is not heating up fast enough, increase the power.
25. Press the center dial to start the heating.
26. Monitor the reaction as the temperature increases; it is now forming lead oleate from the PbO and OA and releasing water, which is then pumped off since the vacuum valve on the Schlenk line is open. The solution should eventually turn from an opaque yellow to clear and colorless.

27. Once the temperature has stabilized at 120 C, leave the reaction for a few hours to make sure all the lead oleate has formed and all water is removed. It's not advisable to leave it for > 5 hours because some further reaction occurs and the solution will turn yellow again, resulting in QDs of poorer quality.

Preparation of TOP-Se precursor:

1. Bring two 20 (24 mL) syringes with purple needles, one 1 mL syringe with a black needle (20G), one vial/small beaker, and the two centrifuge tubes with red caps (for the washing later) into the glovebox.
2. In one 20 mL syringe, withdraw 9.5 mL of TOP-Se solution; try to minimize gas bubbles in the solution.
    a. The day before, check to see if there is already enough solution stored in the glovebox. If not, make a new 1M TOP-Se solution by mixing trioctylphosphine (TOP) with Se shot for 24 hours.
3. Pour out some toluene into the vial/small beaker. Using the other 20 mL syringe, withdraw 10 mL of toluene. Again, minimize the gas bubbles in the syringe.
4. Flip the TOP-Se syringe plunger side down (needle pointing up); you may find it useful to prop it in a test tube holder or something similar. Carefully unscrew the needle.
5. Using the 1 mL syringe, withdraw 0.2 mL of diphenylphosphine (DPP).
6. Insert the 1 mL syringe needle into the TOP-Se solution in the 20 mL syringe via the now open needle port, and inject the DPP.
7. Reattach the purple needle to the TOP-Se syringe. Tip/shake the syringe until the DPP is evenly mixed/distributed in the TOP-Se.

8. DPP is pyrophoric! This isn't a problem in the glovebox or if it exists in dilute solutions, but the 1 mL syringe that was exposed to DPP directly must be rinsed out with the extra toluene from the vial/beaker to properly dilute it so it's safe to bring out of the glovebox. It's good practice to leave all syringes that were exposed to DPP overnight in the fume hood to ensure there isn't any DPP residue before disposing of them in the usual chemical waste container.

QD growth:

1. After waiting for a few hours for the lead oleate to form and the subsequent water to be removed, switch to Ar flow on the Shlenk line and set the J-KEM to 180 C.
2. As the temperature ramps up, you can prepare the Se precursor as outlined in the previous section.
3. Once the reaction reaches 180 C, take the TOP-Se and toluene syringes out of the glovebox.
4. Insert the TOP-Se syringe in the septum of the center neck of the flask. Inject as quickly as possible to ensure uniform nucleation and growth.
5. Allow the dots to grow for 1 min 45 seconds. Prepare a liquid nitrogen bath for quenching the reaction.
6. After 1 min 45 seconds, remove the heating mantle from under the flask and replace it with the liquid nitrogen bath. Turn off the J-KEM so the heating mantle doesn't overheat as the temperature begins to drop.
7. At ~80 C, inject the toluene via the center neck to finish the reaction quench.
8. Remove the flask from the liquid nitrogen bath (if the temperature drops too low, your QD solution will begin to freeze). Remove the thermocouple, close the stopper, and turn off the stir plate/Ar flow/pump.

9. Bring the flask into the box.

QD washing:

1. Inside the box, distribute the QD solution evenly between the two centrifuge tubes. Remove the stir bar using the magnet stuck to the side of the centrifuge.
2. Fill the tubes the rest of the way with acetonitrile and cap.
3. Place the tubes in opposite spots in the centrifuge; check to make sure the compartments have the padded round bottom, not the bare metal bottom (the tubes will break if these are used).
4. Centrifuge at 4400 rpm (4.4 on the display) for 5 min.
5. Decant all of the supernatant into the liquid chemical waste container; there may be a couple liquid layers of varying shades of brown, but a layer of dots should have crashed out at the bottom of each tube.
6. Redisperse the dots in a small amount of toluene (~3 mL). You can use the vortexer/Lab Dancer to make sure all of the layer caked at the bottom of the tube goes into the toluene and doesn't remain stuck on the glass. If the dots are not redispersing, add a little more toluene (overall, less is better).
7. Again, fill the rest of the tubes with acetonitrile, cap, and centrifuge.
8. Repeat steps 5-7 eight more times, for a total of nine washes. The supernatant color should get lighter/clearer, and the dots should get a little easier to redisperse in toluene.
9. After the last wash, put the two centrifuge tubes (loosely capped) into the glovebox antechamber and pump overnight. Alternatively, dry gently with flowing N2, and then leave the tubes uncapped in the glovebox to allow the rest of the solvent to evaporate overnight without any pumping.

10. The dried cake of dots should break into a reasonably dry/crumbly powder. Perform UV-vis characterization and store the dot batch in a closed vial in the glovebox; the shelf life is ~1 year provided that the glovebox is always running at <0.5 ppm O_2.

6.2 EPI-SL FABRICATION VIA INJECTION METHOD

Substrate treatment:

1. To dice/cut Si substrates to desired size (usually at least 1 cm on a side), first score/scratch a straight line on the back side of the Si piece (i.e., the dull side for SSP). Try to make it as deep as possible along the entire length of the desired substrate size.
2. Align the line with the center/white marking on the black clippers/pliers; the substrate should snap cleanly along the line.
3. Repeat until the desired amount of substrates is reached (8-10 is usually a good number).

Substrate cleaning:

1. Place in Teflon (white) substrate holder and place the holder in a beaker; place the beaker in the sonicator after adding the appropriate solvent.

1. First, clean 20-30 min in acetone; once complete, the acetone can be poured into the organic waste container in the fume hood.
2. Then, clean 5-10 min in deionized water (from the white tap to the left of the main sink faucet); once complete, the water can be poured down the drain.
3. Lastly, clean 5-10 min in isopropyl alcohol (IPA / 2-propanol, found in the same cabinet as the acetone); once complete, the IPA can be poured in the “waste IPA” container in the fume hood (purple cap).

4. Retrieve a small petri dish from the QD base bath (if not already in the sink, can be found in the cabinet underneath); use the tongs, or wear the thick black rubber gloves over the normal nitrile ones before reaching into the base bath is recommended (careful, the base bath is essentially an incredibly strong soap, so it's quite slippery!)
5. Rinse the petri dish off with deionized water (remember that the handle doesn't stay in place, so use one hand to constantly turn the knob until rinsing is complete); if the petri dish no longer has soapy bubbles inside of it / no longer feels too slippery, that's probably good enough.
6. Dry the petri dish in the oven (the oven is set to ~110 C, so use protective gloves as needed); usually this takes ~5 min if the dish is turned upside down so that gravity can help drain all of the water droplets out.
7. When the substrates have finished the IPA sonication, take them to the fume hood and dry them with the air gun one by one before placing them into the dried/cleaned petri dish

Substrate treatment:

1. Bring the petri dish with substrates (and lid), an empty vial with white cap, and a container to hold the treated substrates (e.g., a plastic dish; an alternative is to clean/dry another glass petri dish from the base bath if you're afraid of residual toluene that can dissolve the plastic) into the glovebox.

2. Pour ~5 mL of toluene into the petri dish – this is usually enough to fill the bottom of the dish / submerge the substrates. Please wear a pair of nitrile gloves over the glovebox gloves as the toluene will degrade the butyl rubber.

3. Using the blue micropipette, add 120 μL of 3-mercaptopropyltrimethoxysilane (MPTMS) to the toluene; swirl the dish a little bit to mix the solution more thoroughly, but be careful not to splash any out of the dish.
4. Cover the petri dish and let the substrates soak in this solution for at least 45 min (technically, they can be left for as long as a couple of days as long as the dish is covered to prevent toluene evaporation).
5. Remove each substrate from the solution using a pair of tweezers and dunk them directly in a vial of clean toluene; stir them around a little just to make sure all of the excess MPTMS solution is cleaned off.
6. Dry each substrate thoroughly with the N2 gun and deposit them in the substrate container.
7. Clean up consists of bringing the toluene vial and petri dish of MPTMS solution out of the glovebox and dumping the liquids in the organic waste container inside the fume hood. The vial can go into the green chemical waste bucket, and the petri dish should be further rinsed with IPA from the yellow spray bottle (that IPA can go into the organic waste container as well) before being returned to the base bath (recommended at least one overnight soak before reuse).

Acid cleaning of Teflon wells:

Note: Teflon is very soft, so be careful when handling the tray as it can be easily dented, and dents especially along the edge of a well can prevent the glass cover from sealing it properly.

If the Teflon well tray has been soaking in HNO3 (acid):

1. Remove the HNO3 in each well with a 3 mL disposable pipette (in the white cardboard box in the nitrile gloves cabinet by the door) and return to the 5M HNO3 glass bottle in the

acid cabinet underneath the fume hood; the pipette can go into the green chemical waste bucket afterwards.

2. Go next door to Penner lab to use their Millipore water setup at the sink (on the left side of the room once you go through the swinging door by the oven that connects our labs). To start the water flow, step on the white pedal on the floor near the sink.
3. Fill/rinse each well 10x with the water. Try to direct the water stream through the tiny injection holes at the bottom wall of each well.
4. Fill each well one last time with the Millipore water and set the tray aside to soak for at least 20 min. Teflon is quite porous, so the excessive rinsing with water is to give any HNO_3 that might have diffused into the Teflon plenty of opportunity to diffuse back out and avoid contamination of the film fabrication procedure.
5. After a sufficient soak, dump out all the water and do another 5x rinses with Millipore water.
6. Back in our lab, dry the well using the air gun. Make sure there aren't any tiny droplets hiding on the sides or in the corners of any of the wells – this includes the injection holes! It can be tedious to direct the air stream through each of these, but it's very important to make sure there isn't any residual water; otherwise, it will mess up film fabrication later.

Film fabrication:

1. Bring the Teflon tray, an empty vial with white cap, one 10 (12) mL syringe with purple needle, and one 1 mL syringe with black needle into the glovebox.
2. Using the 10 mL syringe, withdraw 7 mL of ethylene glycol (EG) from its secondary container (usually a white-capped vial; if necessary, refill from the brown, red-capped 1L bottle in the glovebox) and deposit it in one of the Teflon wells.

3. Make sure one of the glass covers (parafilm wax covered side facing you) is ready on the side so it can slide into place after depositing the QD solution. Please be careful! The glass covers are fragile and will chip easily.
4. Using the yellow pipette, withdraw 60 μL of QD solution (usually in a tall green-capped vial, made by dissolving QDs in hexanes to the desired concentration, plus vortexing to ensure full dissolution and letting the solution sit at least overnight before use). Remember to depress the button at the top to the first click prior to submerging the tip into the solution; once the tip is submerged, release the button and wait for the solution to finish filling the tip before withdrawing the entire pipette.
5. Deposit the QD solution at the center of the EG surface – it's best to do this drop by drop. Depressing the button on top of the pipette slowly, even prior to the first click, will be enough to start dripping solution from the pipette tip. The idea is to gently deposit the QD solution as one big pool on top of the EG surface.
    a. If the hexane solution somehow breaks through the surface of the EG, it will remain in its own bubble at the bottom of the well and will also be protected from evaporation / won't contribute to film formation on the EG surface.
    b. Hexane evaporates quickly, so the well is covered to extend the evaporation time to ~20 min instead of 20 seconds.
6. Cover the well as quickly as possible. Cap all solutions. The film will take ~20-25 min to form/dry – the pool of QD solution should spread to the sides of the well, and then begin drying from the outside inward. If there is some non-uniform spreading / coverage of the EG surface, the well was likely contaminated, and you should start over with another well.

7. Once the film is dry, uncover the well by using a pair of tweezers to carefully slide off the glass cover.
8. Prepare one of MPTMS-treated substrates by flipping it face down on a clean surface, within easy reach.
9. Fill the empty vial with clean acetonitrile (ACN).
10. Use the 1 mL syringe to withdraw 0.1 mL of EDA solution (made by 1:1 volume ratio of EDA and ACN).
11. Choose a corner of the dried film that has a uniform color/thickness. Submerge the tip of the syringe needle so that it touches the bottom of the well and points underneath the film. It's alright if the film begins to move/crack due to this mechanical disturbance.
12. Inject the EDA as gently as possible. Keep track of the area of film near the injection point.
13. Wait 30 seconds. During this time, prepare to stamp. Depress the button on the side of the vacuum pen and press the suction cup to the back side of the substrate. Once the button is released, the suction should hold the substrate as you move the pen.
14. After 30 seconds, gently lower the substrate (front side facing the QD film) onto the area of film near the injection point. Do not push the substrate past the surface of the EG. As soon as the film makes contact with the front side of the substrate, raise the vacuum pe again; the desired section of film should be removed from the EG surface and stamped onto the substrate.
15. Hold one corner of the substrate + film with a pair of tweezers, and then release the substrate from the vacuum pen (depress the button on the side).
16. Submerge the substrate + film in the clean ACN vial. Again, stir it around to make sure all the excess EG/extra film bits are removed.

17. Dry the substrate using the N2 gun.

Clean up:

1. Bring the Teflon wells, syringes, and ACN vial out of the glovebox.
2. The syringe needles go in the sharps container in the fume hood (box with a flap at the top), and the syringes can go in the green chemical waste bucket.
3. Pour out the ACN in the organic waste container, and throw the vial in the green chemical waste bucket.
4. Using a 3 mL disposable pipette, withdraw all the film/EG from the Teflon wells and deposit in the organic waste container. Throw the pipette in the green chemical waste bucket after.
5. Using Kim wipes (in the small green cardboard boxes scattered around the lab), wipe up the leftover EG/film residue from the wells.
6. Spray the wells with hexane (solid red bottle with downwards facing spray nozzle) and wipe again with the Kim wipes to get as much of the film residue off as possible. Follow this up with IPA if the hexane is not enough to remove all the visible residue.
7. If you still have enough clean wells for another fabrication round, you can store the tray in the drawer and make note of the dirty ones so you don't use them again later. Otherwise, place the tray in the plastic box in the hood with the white lid (labeled with HNO_3) and carefully pour 5M HNO_3 into each of the wells. Cover with the lid and slide the box carefully to the back of the fume hood (spilled acid in the box will mess up the aluminum bottom of the tray even further); at least one overnight soak is recommended before reuse.

6.3 EPI-SL FABRICATION VIA PHOTOBASE METHOD

Substrate cleaning and preparation is the same as described in Section 6.2.

Making the PBG solution:

1. Retrieve the PBG powder, (*E*)-1-Piperdino-3-(20hydroxyphenyl)-2-propen-1-one from FUJIFILM, from the fridge; refrigeration and keeping the vial in the dark reduces its decomposition from exposure to ambient UV light.
2. Measure ~4.6 mg; because the molecular weight is ~231 g/mol, 4.6 mg will make a 1 mM solution in 20 mL of EG, which is enough for 4 films. This can be scaled up or down accordingly, as it's important to bring the powder into the glovebox as quickly as possible.
3. Pump the vial of PBG (loosely capped) and a 20 mL (24 mL) syringe into the glovebox. If a vial of EG isn't already inside, bring another empty vial for that as well.
4. Measure the appropriate amount of EG to make the 1 mM solution from the measured mass of PBG powder.
5. Because this concentration is approaching the maximum solubility of the PBG in EG, vigorous mixing is required (i.e., several minutes of dispersion via the vortexer / Lab Dancer). Once the solution is mostly clear and with no visible particles at the bottom of the vial, wrap the vial in aluminum foil to keep it in the dark and allow the PBG to fully dissolve in the EG overnight before use.

Quartz petri dish cleaning:

1. If no clean quartz petri dishes are already in the glovebox, retrieve the desired number from the quartz-petri-dish-specific base bath (ideally, they should have been soaking for at least a couple of hours).

2. Rinse thoroughly with DI water from the white tap at the base bath sink, i.e., until no more “soapy” bubbles are visible.
3. Dry in oven.
4. Repeat steps 2-3 once more to ensure that all of the base bath residue has been removed from the quartz.
5. When the dishes are completely dry, bring them inside the glovebox for use within the next few days. If they are to be used immediately, make sure they are at room temperature by blow drying them either with the dry air gun by the hoods, or with the nitrogen gun inside the glovebox.

Epi-SL photo-triggered fabrication:

1. Make sure the UV vis lamp is set to the short wave (254 nm) and place it bulb-side up on the glovebox floor; elevate it using the small optic table stands or with some other short piece of material such that the switch won’t be depressed in the lamp’s resting position.
2. Place a clean quartz petri dish on the stand above the UV lamp; the elevation should be ~1.5 cm above the glass cover of the lamp bulb. Because the lamp has both long and short wave, place the dish so that it’s centered over the short-wave bulb as much as possible, i.e., the right side if the lamp is positioned with its handle facing you.
3. Deposit 5 mL of 1 mM PBG in EG inside the dish; this should be just enough to cover the bottom of the dish.
4. Deposit 90 μL of 10 mg/mL QDs in hexanes on the EG surface. Deposit each drop at different points along the circumference of the subphase surface, as near the dish walls as possible; because quartz is hydrophilic (and for reasons described in Chapter 3.3), the QD solution won’t spread well if it’s deposited at the center.

5. Cover immediately with a petri dish lid that has an O-ring epoxied inside of it. If a new one is needed, make sure both the O-ring and the epoxy are chemically resistant.
6. Once the film has dried (~10 min), lift the cover and check for thickness using the reflection from the white overhead light for this; the film reflection should be gold for a ~60 nm film.
7. Plug in the UV lamp for 1 hour to allow generation of the photobase before unplugging again.
8. Allow the film to exchange for 4 more hours in the dark.
9. Stamp the desired area with substrate of choice, clean thoroughly with fresh acetonitrile, and dry with flowing nitrogen.

6.4 NORMALIZED OLEATE REMOVAL CALCULATION AND ANALYSIS

Accurately calculating the % oleate (OA) removal is a process with several components. Before beginning the procedure, ensure that the proper 0 % oleate removal CH area (i.e., the OA reference) is already determined. This process only works if all measured samples are the same thickness (visually, can be discerned by reflection color on the same type of substrate). If the film is of a different thickness, you will need to retake the OA reference for that thickness and fill in the appropriate values in the green cells of the "FTIR + coverage" and "SEM + final" tabs of the "oleate removal calculator.xlsx" spreadsheet.

The quantification is split into three parts: substrate coverage correction, glycoxide + oleate model fitting of the FTIR spectrum, and densification correction, briefly detailed in Figure 6.1. The following procedure assumes possession of the above-mentioned spreadsheet, as well as the Igor procedure files "area.ipf", "Baselines_2.ipf", "Color6.ipf", "FET_IV_V5.ipf", "FTIR.ipf".

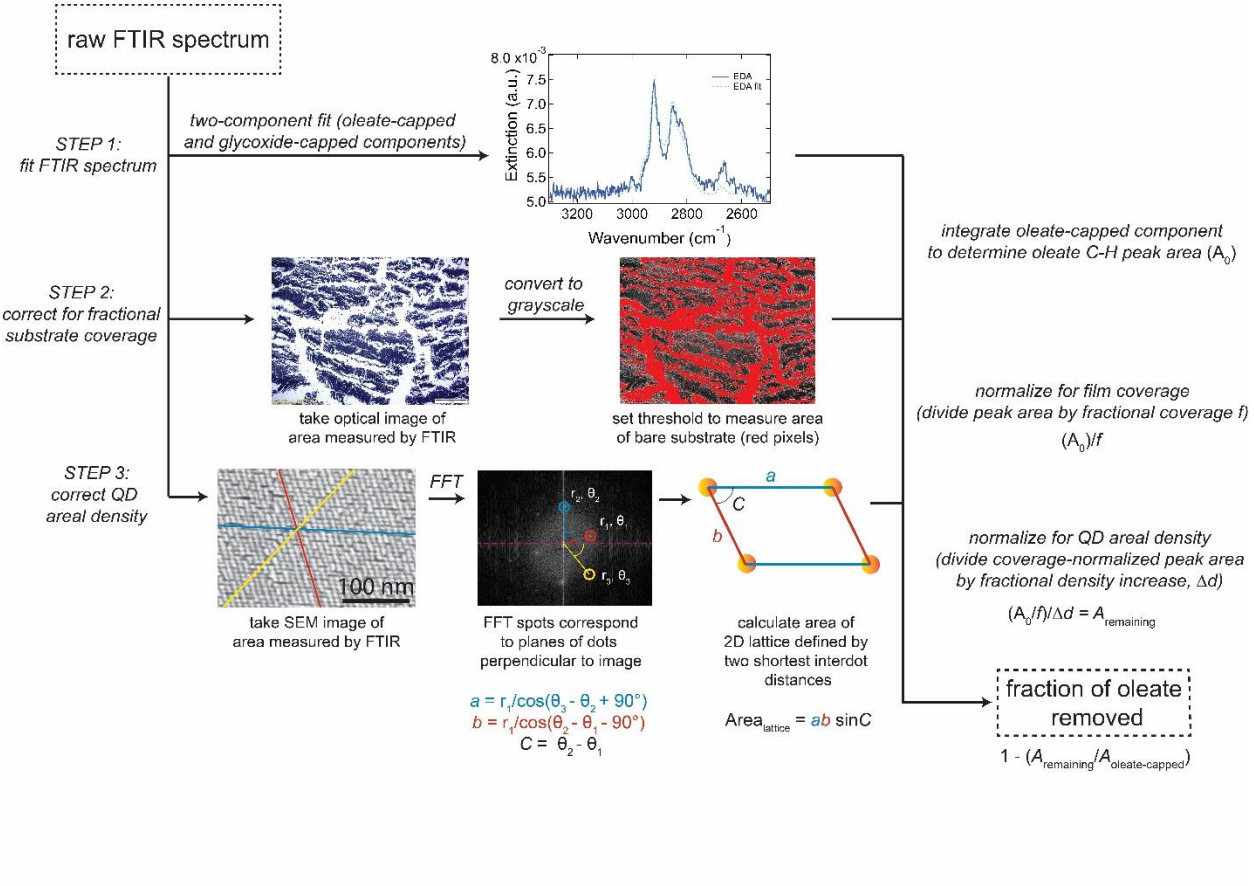

Figure 6.1: *Flow chart of the normalized oleate removal calculation process. Reprinted with permission from ACS Nano 2022, 16, 2, 3239-3250. Copyright 2022 American Chemical Society.*

Substrate coverage correction:

1. Use the optical microscope in Javier Sanchez-Yamagishi's lab in the Rowland Hall basement to take images of the same area of the sample exposed by the FTIR window. Use the 2.5x magnification to image the entire area in one go; otherwise use the 5x lens and stitch four images together of the same area. The rest of this procedure is with the 2.5x magnification in mind, but for the 5x be aware that you have to sum up the four separate areas appropriately to get the final coverage.
2. On your computer, open ImageJ, and then the first image you would like to analyze.

3. Use the line tool in the menu tool bar to click and drag a line along the scale bar at the bottom right of the image (hold down the shift key as you drag to keep the line perfectly horizontal).
4. Go to Analyze ≫ Set Scale. In “known distance”, input the corresponding value from the scale bar label. Click OK.
5. Next go to Image ≫ Type ≫ 8-bit to convert the image into grayscale.
6. Use the rectangle tool to select the entire image (you can leave out the scalebar portion). Hit ctrl+M to measure the area enclosed by this rectangle. This value is the “total area” in the “FTIR + coverage” tab of the “oleate removal calculator.xlsx” spreadsheet.
7. Hit ctrl+shift+T to threshold the image. You can adjust the sliding bars in the threshold window so that all of the red pixels cover only the areas of the bare substrate.
8. Hit ctrl+M again; this time the area that pops up should be of just the red pixels. If this doesn’t seem to be the case, go to Analyze ≫ Set Measurements and make sure “Limit to Threshold” is checked. This new area goes into the “threshold area” cell in the spreadsheet.

Glycoxide fitting:

1. Open the “FTIR fitting.pxp” Igor Pro file and Save As the desired file name. The “FTIR fitting.pxp” file comes with the model spectra already included, always start working from this.
2. Type **ftir()** into the command bar. This will call a dialogue box for you to input the wavenumber range of the data you want to import. Normally our data range is 7000 to 500 cm^{-1}, so you can type those into the final and initial boxes, respectively (remember we go from highest to lowest, just because of convention).

3. In the next window, navigate to the appropriate folder and select the data you want to look at. You can select multiple files in the same folder using ctrl+click, but if you have files in a different folder, you will have to run the ftir() command again to plot those.
4. After you've finished running the ftir() command, you should have a window with all of your data plotted. If you had to run ftir() more than once, you can right click on any of the white space of your target graph and select "Append Traces to Graph". You will need to know the wave names of the traces you want to append (e.g., wave3). Remember that the wave you select on the left column will define the y axis, and the wave you select on the right column will define the x.
5. Go to "Macros" on the menu bar and select "Baselines". This will correct for any sloping we see in the background of the spectrum. First select the wave you want to correct, and then select "spline" from the baseline type dropdown menu. You can then highlight the regions of the spectrum you want to anchor the fit around and adjust the spline coefficient as necessary. Remember that you want a nice flat baseline, particularly in the CH region of interest. Click "subtract" once you're satisfied.
6. After your baseline is adjusted, hit ctrl+I to bring up the info box at the bottom of your graph. You can click and drag cursors A and B onto the plot (make sure they're both sitting on the same wave; you can right click on the displayed wave name next to each cursor and select the wave you want); A should be at pnt 1346 (~3095 cm^{-1}) and B should be at pnt 1152 (~2721 cm^{-1}) if you collected your data at a resolution of 4 cm^{-1}.
7. In "Macros", select "Area XY Between Cursors". Your area will then be produced in the command window. This is the area that goes into the "FTIR area (y)" column of your spreadsheet.

8. In the Igor Pro command window, type **duplicate wave_sub, wave_raw**. In this case, wave_sub is the wave name of your baseline corrected data, and wave_raw is a copy of it (these wave names are just stand ins for the instructions; you can choose whichever names you want for your own data). We want to save a copy of the original because we are going to be adjusting the wave_sub spectrum now.
9. Copy the number in the "area ratio (corrected:measured)" cell of the spreadsheet. In Igor Pro, type **wave_sub = wave_sub*[number]** where [number] is the value you just copied. This will scale up the wave_sub spectrum to correct for the incomplete substrate coverage.
10. Go to Windows ≫ New Graph and append wave_sub, **fitsum**, **fit1s**, and **fitOAs** with their appropriate x axes (fitsum, fit1s, and fitOAs can be paired with _calculated_).
11. Now, adjust fit1s and fitOAs in the command bar by typing different [number] values with **fit1s = [number]*fit_wave1_smth_sub** and **fitOAs = [number]*fit_OA** until the two components seem to match the wave_sub spectrum. Remember that fit1s is the glycoxide component and fitOAs is the oleate component of the model.
12. To add the two separate components together, type **SumWaves(fitsum, "fitOAs;fit1s;")** into the command bar. Now the fitsum curve should look like the sum of the fitOAs and fit1s components.
13. Pull up the info box again (ctrl+I) and drag the A and B cursors to fitsum. Adjust them so that A is on pnt 443 and B is on pnt 178 (the wavenumbers should roughly match the range at which you measured the wave_sub area, i.e. 3095 and 2721). Use "Area XY Between Cursors" to measure this area and see how it compares to the value in the "corrected FTIR area" cell in your spreadsheet.

14. If you think the numbers are a close match (typically within 0.01 is good), copy the fitsum area into the “model area” cell in the spreadsheet.
15. Move the A and B cursors to fit1s; A should be on pnt 315 and B should be on pnt 127; (again, they should be roughly on the same wavenumber range as the previous two areas you’ve measured). Use “Area XY Between Cursors” and paste the value into “corrected glycoxide area” in the spreadsheet.
16. Check the “corrected glycoxide area error” cell. If the value is more than 0.005, repeat steps 11 – 15 until the error is < 0.005. Of course, the fitsum spectrum should roughly match the wave_sub spectrum visually as well.
17. Once this is complete, type **duplicate fitsum, fitsumA**, where fitsumA is a copy of this fit and frees the original fitsum wave to be adjusted to a new spectrum later.
18. Go to Windows ≫ New ≫ Notebook to open a blank text file. You can use this to record the coefficients of fit1s and fitOAs in case you need to refer to them later.

Densification correction:

1. Open ImageJ.
2. Open the appropriate SEM image of your film.
3. Set the scale bar as you did in Part 1.
4. Go to Process ≫ FFT ≫ FFT. This should give you a black image with a pattern of six white spots around the center in a vague hexagon configuration. If the white spots are too diffuse/blurred/faint, you can use the rectangle or oval tool to select a more pristine region of the image (ideally, no cracks/boundaries) to analyze.
5. Imagine the FFT image split into quadrants like a normal Cartesian coordinate plot. In quadrant I (i.e., positive y and positive x), find the spot closest to the positive x axis. Hover

your cursor over as close to the center of this spot as possible (ctrl + scroll will zoom in towards wherever your cursor is located and can enable a more accurate selected center). Values for "r="and "theta=" will pop up under the menu tool bar; enter these into the "d1" and "theta1" cells, respectively, in the "SEM + final" tab in your spreadsheet.

   a. Note that the r and theta values will change as soon as you move your mouse. Fortunately, you can have Excel be the active application and still hover your mouse over the FFT image to display the values you need to type in; thus, this process is much easier with dual monitors, or at least a split screen.

6. Continue counterclockwise around the image for d2/theta2 and d3/theta3. The other three spots are just 180-degree reflections of the first three, so you don't need to bother with those.
7. Note the values in the r1/r2/r3 columns of the spreadsheet. Determine the two shortest directions (it helps to bold or otherwise highlight these two values because you will need to use them later) and adjust the formula in the "phi" cell according to the green table at the top left of the sheet.
8. Repeat steps 2-7 for all available SEM images of your sample.
9. In column M of the spreadsheet ("long side"), average the values of the <u>longer</u> short direction for all the images (**=AVERAGE(cell1, cell2, cell3, …)**) in the bolded row. Directly underneath will be the un-bolded row for error calculations; in this, you can use the exact same cells but do the standard deviation (**=STDEV(cell1, cell2, cell3, …)**).
10. Repeat step 9 for column O ("short side", i.e., the <u>shorter</u> of the two short directions) and column P ("angle").

11. In column T (“FTIR”), make sure that it references the corresponding “oleate remaining” cell (column P) for the same sample on the “FTIR + coverage” tab.
12. Your final % OA removal is displayed in column V of the “SEM + final” tab.

BIBLIOGRAPHY

(1) Kagan, C. R.; Lifshitz, E.; Sargent, E. H.; Talapin, D. V. Building Devices from Colloidal Quantum Dots. *Science* **2016**, *353* (6302). https://doi.org/10.1126/science.aac5523.

(2) Nozik, A. J.; Beard, M. C.; Luther, J. M.; Law, M.; Ellingson, R. J.; Johnson, J. C. Semiconductor Quantum Dots and Quantum Dot Arrays and Applications of Multiple Exciton Generation to Third-Generation Photovoltaic Solar Cells. *Chem. Rev.* **2010**, *110* (11), 6873–6890. https://doi.org/10.1021/cr900289f.

(3) Hu, L.; Zhang, Z.; Patterson, R. J.; Shivarudraiah, S. B.; Zhou, Z.; Ng, M.; Huang, S.; Halpert, J. E. PbSe Quantum Dot Passivated Via Mixed Halide Perovskite Nanocrystals for Solar Cells With Over 9% Efficiency. *Sol. RRL* **2018**, *2* (12), 1800234. https://doi.org/10.1002/solr.201800234.

(4) *Colloidal Quantum Dot Optoelectronics and Photovoltaics*; Konstantatos, G., Sargent, E., H., Eds.; Cambridge University Press, 2013.

(5) Evers, W. H.; Goris, B.; Bals, S.; Casavola, M.; de Graaf, J.; van Roij, R.; Dijkstra, M.; Vanmaekelbergh, D. Low-Dimensional Semiconductor Superlattices Formed by Geometric Control over Nanocrystal Attachment. *Nano Lett.* **2013**, *13* (6), 2317–2323. https://doi.org/10.1021/nl303322k.

(6) Lambert, K.; Čapek, R. K.; Bodnarchuk, M. I.; Kovalenko, M. V.; Van Thourhout, D.; Heiss, W.; Hens, Z. Langmuir−Schaefer Deposition of Quantum Dot Multilayers. *Langmuir* **2010**, *26* (11), 7732–7736. https://doi.org/10.1021/la904474h.

(7) Dong, A.; Chen, J.; Vora, P. M.; Kikkawa, J. M.; Murray, C. B. Binary Nanocrystal Superlattice Membranes Self-Assembled at the Liquid–Air Interface. *Nature* **2010**, *466* (7305), 474–477. https://doi.org/10.1038/nature09188.

(8) Josten, E.; Wetterskog, E.; Glavic, A.; Boesecke, P.; Feoktystov, A.; Brauweiler-Reuters, E.; Rücker, U.; Salazar-Alvarez, G.; Brückel, T.; Bergström, L. Superlattice Growth and Rearrangement during Evaporation-Induced Nanoparticle Self-Assembly. *Sci. Rep.* **2017**, *7* (1), 2802. https://doi.org/10.1038/s41598-017-02121-4.

(9) Abelson, A.; Qian, C.; Salk, T.; Luan, Z.; Fu, K.; Zheng, J.-G.; Wardini, J. L.; Law, M. Collective Topo-Epitaxy in the Self-Assembly of a 3D Quantum Dot Superlattice. *Nat. Mater.* **2020**, *19*, 49–55. https://doi.org/10.1038/s41563-019-0485-2.

(10) Chu, X.; Heidari, H.; Abelson, A.; Unruh, D.; Hansen, C.; Qian, C.; Zimanyi, G.; Law, M.; Moulé, A. J. Structural Characterization of a Polycrystalline Epitaxially-Fused Colloidal Quantum Dot Superlattice by Electron Tomography. *J. Mater. Chem. A* **2020**, *8* (35), 18254–18265. https://doi.org/10.1039/D0TA06704K.

(11) Whitham, K.; Yang, J.; Savitzky, B. H.; Kourkoutis, L. F.; Wise, F.; Hanrath, T. Charge Transport and Localization in Atomically Coherent Quantum Dot Solids. *Nat. Mater.* **2016**, *15* (5), 557–563. https://doi.org/10.1038/nmat4576.

(12) Walravens, W.; De Roo, J.; Drijvers, E.; ten Brinck, S.; Solano, E.; Dendooven, J.; Detavernier, C.; Infante, I.; Hens, Z. Chemically Triggered Formation of Two-Dimensional Epitaxial Quantum Dot Superlattices. *ACS Nano* **2016**, *10* (7), 6861–6870. https://doi.org/10.1021/acsnano.6b02562.

(13) Alimoradi Jazi, M.; Kulkarni, A.; Sinai, S. B.; Peters, J. L.; Geschiere, E.; Failla, M.; Delerue, C.; Houtepen, A. J.; Siebbeles, L. D. A.; Vanmaekelbergh, D. Room-Temperature Electron Transport in Self-Assembled Sheets of PbSe Nanocrystals with a Honeycomb Nanogeometry. *J. Phys. Chem. C* **2019**, *123* (22), 14058–14066. https://doi.org/10.1021/acs.jpcc.9b03549.

(14) Liu, Y.; Tolentino, J.; Gibbs, M.; Ihly, R.; Perkins, C. L.; Liu, Y.; Crawford, N.; Hemminger, J. C.; Law, M. PbSe Quantum Dot Field-Effect Transistors with Air-Stable Electron Mobilities above 7 Cm2 V–1 s–1. *Nano Lett.* **2013**, *13* (4), 1578–1587. https://doi.org/10.1021/nl304753n.

(15) Wu, Y.; Li, S.; Gogotsi, N.; Zhao, T.; Fleury, B.; Kagan, C. R.; Murray, C. B.; Baxter, J. B. Directional Carrier Transfer in Strongly Coupled Binary Nanocrystal Superlattice Films Formed by Assembly and in Situ Ligand Exchange at a Liquid–Air Interface. *J. Phys. Chem. C* **2017**, *121* (8), 4146–4157. https://doi.org/10.1021/acs.jpcc.6b12327.

(16) Crisp, R. W.; Kroupa, D. M.; Marshall, A. R.; Miller, E. M.; Zhang, J.; Beard, M. C.; Luther, J. M. Metal Halide Solid-State Surface Treatment for High Efficiency PbS and PbSe QD Solar Cells. *Sci. Rep.* **2015**, *5* (1), 1–6. https://doi.org/10.1038/srep09945.

(17) Anderson, N. C.; Hendricks, M. P.; Choi, J. J.; Owen, J. S. Ligand Exchange and the Stoichiometry of Metal Chalcogenide Nanocrystals: Spectroscopic Observation of Facile Metal-Carboxylate Displacement and Binding. *J. Am. Chem. Soc.* **2013**, *135* (49), 18536–18548. https://doi.org/10.1021/ja4086758.

(18) Qian, C.; Abelson, A.; Miller-Casas, A.; Capp, R.; Vinogradov, I.; Udagawa, N. S.; Ge, N.-H.; Law, M. Photobase-Triggered Formation of 3D Epitaxially Fused Quantum Dot Superlattices with High Uniformity and Low Bulk Defect Densities. *ACS Nano* **2022**, *16* (2), 3239–3250. https://doi.org/10.1021/acsnano.1c11130.

(19) Kagan, C. R.; Murray, C. B. Charge Transport in Strongly Coupled Quantum Dot Solids. *Nat. Nanotechnol.* **2015**, *10* (12), 1013–1026. https://doi.org/10.1038/nnano.2015.247.

(20) Kalesaki, E.; Evers, W. H.; Allan, G.; Vanmaekelbergh, D.; Delerue, C. Electronic Structure of Atomically Coherent Square Semiconductor Superlattices with Dimensionality below Two. *Phys. Rev. B* **2013**, *88* (11), 115431. https://doi.org/10.1103/PhysRevB.88.115431.

(21) Chapter 5 - Bandstructure and Related Properties. In *Semiconductors and Semimetals*; Jain, S. C., Willander, M., Eds.; Silicon-Germanium Strained Layers and Heterostructures; Elsevier, 2003; Vol. 74, pp 91–145. https://doi.org/10.1016/S0080-8784(03)80018-2.

(22) Balazs, D. M.; Matysiak, B. M.; Momand, J.; Shulga, A. G.; Ibáñez, M.; Kovalenko, M. V.; Kooi, B. J.; Loi, M. A. Electron Mobility of 24 Cm2 V−1 S−1 in PbSe Colloidal-Quantum-Dot Superlattices. *Adv. Mater.* **2018**, *30* (38), 1802265. https://doi.org/10.1002/adma.201802265.

(23) Choi, H. H.; Cho, K.; Frisbie, C. D.; Sirringhaus, H.; Podzorov, V. Critical Assessment of Charge Mobility Extraction in FETs. *Nat. Mater.* **2018**, *17* (1), 2–7. https://doi.org/10.1038/nmat5035.

(24) Alimoradi Jazi, M.; Janssen, V. A. E. C.; Evers, W. H.; Tadjine, A.; Delerue, C.; Siebbeles, L. D. A.; van der Zant, H. S. J.; Houtepen, A. J.; Vanmaekelbergh, D. Transport Properties of a Two-Dimensional PbSe Square Superstructure in an Electrolyte-Gated Transistor. *Nano Lett.* **2017**, *17* (9), 5238–5243. https://doi.org/10.1021/acs.nanolett.7b01348.

(25) Jang, J.; Liu, W.; Son, J. S.; Talapin, D. V. Temperature-Dependent Hall and Field-Effect Mobility in Strongly Coupled All-Inorganic Nanocrystal Arrays. *Nano Lett.* **2014**, *14* (2), 653–662. https://doi.org/10.1021/nl403889u.

(26) Pourret, A.; Guyot-Sionnest, P.; Elam, J. W. Atomic Layer Deposition of ZnO in Quantum Dot Thin Films. *Adv. Mater.* **2009**, *21* (2), 232–235. https://doi.org/10.1002/adma.200801313.

(27) Zarghami, M. H.; Liu, Y.; Gibbs, M.; Gebremichael, E.; Webster, C.; Law, M. P-Type PbSe and PbS Quantum Dot Solids Prepared with Short-Chain Acids and Diacids. *ACS Nano* **2010**, *4* (4), 2475–2485. https://doi.org/10.1021/nn100339b.

(28) Balazs, D. M.; Dirin, D. N.; Fang, H.-H.; Protesescu, L.; ten Brink, G. H.; Kooi, B. J.; Kovalenko, M. V.; Loi, M. A. Counterion-Mediated Ligand Exchange for PbS Colloidal Quantum Dot Superlattices. *ACS Nano* **2015**, *9* (12), 11951–11959. https://doi.org/10.1021/acsnano.5b04547.

(29) McCray, A. R. C.; Savitzky, B. H.; Whitham, K.; Hanrath, T.; Kourkoutis, L. F. Orientational Disorder in Epitaxially Connected Quantum Dot Solids. *ACS Nano* **2019**, *13* (10), 11460–11468. https://doi.org/10.1021/acsnano.9b04951.

(30) Momper, R.; Zhang, H.; Chen, S.; Halim, H.; Johannes, E.; Yordanov, S.; Braga, D.; Blülle, B.; Doblas, D.; Kraus, T.; Bonn, M.; Wang, H. I.; Riedinger, A. Kinetic Control over Self-Assembly of Semiconductor Nanoplatelets. *Nano Lett.* **2020**, *20* (6), 4102–4110. https://doi.org/10.1021/acs.nanolett.9b05270.

(31) Wang, Y.; Peng, X.; Abelson, A.; Xiao, P.; Qian, C.; Yu, L.; Ophus, C.; Ercius, P.; Wang, L.-W.; Law, M.; Zheng, H. Dynamic Deformability of Individual PbSe Nanocrystals during Superlattice Phase Transitions. *Sci. Adv. 5* (6), eaaw5623. https://doi.org/10.1126/sciadv.aaw5623.

(32) Kavrik, M. S.; Hachtel, J.; Ko, W.; Qian, C.; Abelson, A.; Unlu, E. B.; Kashyap, H.; Li, A.-P.; Idrobo, J.-C.; Law, M. *Emergence of Distinct Electronic States in Epitaxially-Fused PbSe Quantum Dot Superlattices*; preprint; In Review, 2021. https://doi.org/10.21203/rs.3.rs-841852/v1.

(33) Balazs, D. M.; Erkan, N. D.; Quien, M.; Hanrath, T. Inkjet Printing of Epitaxially Connected Nanocrystal Superlattices. *Nano Res.* **2021**. https://doi.org/10.1007/s12274-021-4022-7.

(34) Chen, W.; Tang, H.; Chen, Y.; Heger, J. E.; Li, N.; Kreuzer, L. P.; Xie, Y.; Li, D.; Anthony, C.; Pikramenou, Z.; Ng, K. W.; Sun, X. W.; Wang, K.; Müller-Buschbaum, P. Spray-Deposited PbS Colloidal Quantum Dot Solid for near-Infrared Photodetectors. *Nano Energy* **2020**, *78*, 105254. https://doi.org/10.1016/j.nanoen.2020.105254.

(35) Nie, H.-L.; Dou, X.; Tang, Z.; Jang, H. D.; Huang, J. High-Yield Spreading of Water-Miscible Solvents on Water for Langmuir–Blodgett Assembly. *J. Am. Chem. Soc.* **2015**, *137* (33), 10683–10688. https://doi.org/10.1021/jacs.5b06052.

(36) Balazs, D. M.; Dunbar, T. A.; Smilgies, D.-M.; Hanrath, T. Coupled Dynamics of Colloidal Nanoparticle Spreading and Self-Assembly at a Fluid–Fluid Interface. *Langmuir* **2020**, *36* (22), 6106–6115. https://doi.org/10.1021/acs.langmuir.0c00524.